Sensitivity of the ORCA neutrino detector to quantum decoherence effects

Research oriented project

Max Joseph Fahn
02. February 2019

Friedrich-Alexander-University Erlangen-Nürnberg

Supervisor:

PD Dr. Thomas Eberl

Abstract

The discovery of neutrino oscillations around the year 2000 gave new insights into particle physics. In addition, it also opened up new avenues for future developments in physics. For example, it is possible to study decoherence effects that alter the oscillations. Along these lines, we used a simple model for decoherence and studied how this influences propagation of neutrinos. We further made sensitivity analyses for the neutrino detector ORCA to see whether the above influence can be detected. The result of our analyses shows that such decoherence processes do have a non-negligible effect on the oscillation probabilities and that they are also measurable by ORCA. So, the focus can now shift to theories that try to explain these decoherence effects. Hot candidates are quantum gravity theories like the loop quantum gravity.

Acknowledgements

I want to thank **PD Dr. Thomas Eberl** for giving me this great project and the opportunity to work in the center of neutrino research as a newcomer to this topic. I highly appreciate the great freedom I was given to push the project into my preferred direction. I am thankful for the great support I received during all my time at the institute and for all the fruitful discussions.

I also want to thank **Marc Bruchner** for his great introduction to paramNMH and his help with the program which saved me a lot of time.

I would also like to extend my thanks to **Dr. Jannik Hofestädt** for the helpful discussions and comments on the project and this report.

Contents

1 Puzzles in neutrino physics

The effort of human beings to understand our universe has led to the discovery of many different particles. At first, electrically charged and particles with mass clearly greater than zero turned up in theory and experiments. But apart from these particles, also particles without electric charge and with very little mass exist. Their discovery took a much longer time. So was the most prominent and interesting of these particles, the neutrino, first measured in 1956 [1]. As it only participates in weak interactions (its masses are negligible small or zero), it can only be measured by detecting secondary particles created by an interaction of a neutrino with matter.

While the neutrino was postulated in 1930 in a letter by Wolfgang Pauli in order to achieve energy conservation in weak decays [2], the first one to publish such postulate was Enrico Fermi a few years later [3, 4]. Theoretical investigations resulted in three neutrino flavours that can take part in weak interactions, each related to one of the three lepton families. Apart from these flavours, which are known today, also further 'sterile' neutrinos without weak charge could exist. As these sterile neutrinos do (almost) not interact with standard matter, it is very difficult to prove their existence today. Early assumptions considered the neutrino to be a massless particle. This assumption led to a period in neutrino physics which was dominated by a puzzle that made scientists rethink their knowledge of neutrinos, the sun and experimental methods: the solar neutrino puzzle. When in the mid-1960s the first values for the solar flux of neutrinos were measured by R. Davis and his group (see [5] and [6]), a discrepancy between the theoretically expected and the measured value was observed, which amounted to more than 70 percent. In the following decades, several experiments confirmed this deviation from experimental and theoretical values [7]. In the next almost 40 years different attempts to solve this puzzle had been carried out (see for example [8], [9] and [10]).

In 2002 one of these theories, the theory of neutrino oscillations, was experimentally confirmed [11]. Measuring not only electron neutrinos, which are generated in the sun, but also muon and tau neutrinos, which are not generated in the sun and adding up all three fluxes gives the expected flux of electron neutrinos from the sun. The explication for that is simple from today's point of view: Considered as quantum particles, neutrinos interact in their flavour basis, but propagate in their mass basis. This leads to oscillations between the different flavours during propagation, so an electron neutrino created in the sun may be measured as a muon neutrino when it reaches the earth. The oscillation parameters depend on different quantities like energy of the neutrino, its propagation length and other fixed but today not known parameters like the masses of the neutrinos and their mixing angles (that is the exact relation between the mass and flavour basis).

Enormous efforts are taken on to determine these inherent parameters (the most recent values can be found at [12]). This effort is required, because reactions of neutrinos with matter occur very rarely despite the huge neutrino flux on earth from different sources, which is more than 65 billion neutrinos per second and cm^2. From that issue arises the

necessity of building large detectors to measure neutrinos along with their energy and direction. One of these detectors being built is the Cubic Kilometre Neutrino Telescope, in short KM3NeT ([13], [14]). It consists of two parts spread over the Mediterranean Sea. One of them, the ORCA detector (Oscillation Research with Cosmics in the Abyss), aims on a better measurement of neutrino oscillations than it is possible with already built detectors.

Nevertheless, without an appropriate model the data might be misinterpreted. The usual model of neutrino oscillations today does not take into account dependencies aside from the above named ones, which contain the energy of the neutrino, its propagation length, its masses and the mixing angles. But also an influence of non-classical decoherence effects on a neutrino system is possible. Reasons for such non-classical decoherence effects may arise for example from quantum gravity. Including this decoherence leads to modified formulas for the oscillation and therefore may also give modified values of the standard oscillation parameters. Due to this fact, it is highly important to consider decoherence as early as possible if it is of a sufficient order of magnitude, such that it makes us interpret the experimental data wrong. An interesting analysis concerning this topic is presented in [15], where experimental differences measured for an oscillation parameter are found to be explainable by decoherence effects arising in different baseline lengths of the considered detectors.

In this project, we will investigate this non-classical decoherence effects in a three-flavour model for neutrinos and test the sensitivity of ORCA for these effects. After introducing the relevant theory in section 2, we will discuss the ORCA detector and its performance in section 3. Then, we will introduce the software used to perform the analyses and describe our setup in section 4. In section 5, we present our results and discuss them. Finally, we will give an outlook in section 6. In contrary to several performed analyses that used a two flavour picture (see for example [16], [17], [18] or [19]), we will perform our analysis with the full three flavour picture ([15], [20] and [21]).

2 Theory of Neutrino Oscillations

In this section, we discuss the phenomenological basics for neutrino oscillations. We start with time evolution of a neutrino system in vacuum. As a next step, we take into account matter effects and show, how they modify oscillations. In the second part, we make a phenomenological approach to decoherence and include decoherence effects into our evolution equations. The derivations will be close to [22].

2.1 Standard Oscillations

For our calculations, we will consider three interacting neutrino flavours. As already mentioned, neutrinos propagate in the mass basis and interact in the flavour basis. Due to reasons of conserved probability, the two bases are connected to each other with a unitary transformation U. Labeling the flavour states with $|\nu_\alpha\rangle$ and the mass states with $|\nu_i\rangle$, this gets

$$|\nu_\alpha\rangle = \sum_{i=1}^{3} U_{\alpha i} \, |\nu_i\rangle \ . \tag{1}$$

The matrix $U_{\alpha i}$ is also called the PMNS-matrix and can be decomposed into a product of four matrices. These matrices contain three angles, one complex phase δ_{CP}, which violates the CP-invariance if it is not zero, and two additional Majorana phase factors, which are unimportant for our later purposes as they do not interfere with neutrino oscillations.
As a next step, we will treat time evolution of the neutrino. For that, we choose to work in the density matrix formalism. This is a reasonable choice, because using that formalism it is possible to model evolution of a pure state into a mixed state. This process, even though it is forbidden by standard quantum mechanics, is apparent in nature: Black holes, which initially are in a pure states, may vanish after a certain time and dissolve into thermal Hawking radiation. Microscopic, short-lived black holes can arise out of vacuum and undergo such a transition from a pure to a mixed state. Density matrix formalism with an extended time evolution equation (which we will introduce in the next section) is capable of such transitions. The basic time evolution is given by the Liouville-von Neumann equation:

$$\partial_t \rho = -i[H, \rho] \ , \tag{2}$$

with H denoting the Hamiltonian of our neutrino system. In vacuum, it has the form

$$H_{vac} = diag\{E_1, E_2, E_3\} \ . \tag{3}$$

The energies E_i correspond to the mass eigenstates m_i of the neutrinos. Equation (2) is a first order, linear and homogeneous differential equation. To find a solution, we first

expand all operators in the following basis:

$$F_0 = \frac{1}{\sqrt{3}} I_3 \quad F_j = \frac{1}{\sqrt{2}} \Lambda_j \ . \tag{4}$$

This basis is defined by the identity I_3 and the Gell-Mann matrices $(\Lambda_j)_{\{j=1,\dots,8\}}$, which form a representation for the infinitesimal generators of the SU(3), fulfilling

$$[\Lambda_i, \Lambda_j] = \sum_k i f_{ijk} \Lambda_k \ . \tag{5}$$

In this basis we expand an operator O according to

$$O = \sum_{i=0}^{8} Tr(O F_i) F_i \ , \tag{6}$$

as the nine matrices F_i form an orthonormal basis set with respect to the scalar product

$$\langle F_i | F_j \rangle := Tr[F_i F_j] = \delta_{ij} \ , \tag{7}$$

which can easily be verified using the explicit representation of the Gell-Mann matrices given in [23]. Expanding both sides of equation (2) in this basis gives as prefactor in front of F_j on the left hand side

$$Tr((\partial_t \rho) F_j) = \partial_t Tr(\rho F_j) =: \partial_t \rho_j \tag{8}$$

and on the right hand side

$$Tr((-i[H, \rho]) F_j) = -i\, Tr([H, \rho] F_j) \ . \tag{9}$$

Next, expanding H and ρ in terms of the expansion (6) yields

$$= \sum_{i,k} -i\, Tr([Tr(HF_i)F_i, Tr(\rho F_k)F_k]F_j) = \sum_{i,k} -i\, Tr(HF_i)\, Tr(\rho F_k)\, Tr([F_i, F_k]F_j) \ . \tag{10}$$

Continuing with equality (5), which generalises to the F_j, we get

$$= \sum_{i,k,m} Tr(HF_i)\, \rho_k\, f_{ikm}\, Tr(F_m F_j) = \sum_{i,k} Tr(HF_i)\, f_{ikj}\, \rho_k =: \sum_k \left(\tilde{H}\right)_{jk} \rho_k \ . \tag{11}$$

So we derived

$$\partial_t \vec{\rho} = \tilde{H} \vec{\rho} \tag{12}$$

with $\rho_j = Tr(\rho F_j)$ and $\left(\tilde{H}\right)_{ij} = \sum_l Tr(HF_l)\, f_{lji}$. This is a system of nine first order linear differential equations, so it can be solved by matrix exponentiation:

$$\vec{\rho}(t) = exp(\tilde{H}) \cdot \vec{\rho}(0) \ . \tag{13}$$

This exponentiation can be computed straight forwardly for a given Hamiltonian H. Technically, its computation time can be improved by diagonalising $\tilde{H} =: T\tilde{H}_D T^{-1}$, then (13) can be evaluated as

$$\vec{\rho}(t) = T \cdot exp(\tilde{H}_D) \cdot T^{-1} \cdot \vec{\rho}(0) \ . \tag{14}$$

For the vacuum Hamiltonian (3), it turns out that $\tilde{H}_{vac}$ is block diagonal and each block depends only on energy differences $\Delta_{ij} := E_i - E_j$. The result obtained in this case is

$$\rho(t) = \sum_i \rho_i(t)\, F_i = \begin{pmatrix} \rho_{11}(0) & \rho^*_{21}(0)\, e^{i\Delta_{21}t} & \rho^*_{31}(0)\, e^{i\Delta_{31}t} \\ \rho_{21}(0)\, e^{-i\Delta_{21}t} & \rho_{22}(0) & \rho^*_{32}(0)\, e^{i\Delta_{32}t} \\ \rho_{31}(0)\, e^{-i\Delta_{31}t} & \rho_{32}(0)\, e^{-i\Delta_{32}t} & \rho_{33}(0) \end{pmatrix} \ . \tag{15}$$

The expression to get the probability of measuring a certain neutrino flavour β at time t if flavour α has been created at time $t_0 = 0$ is given by

$$P_{\alpha\to\beta} = |\, \langle \nu_\alpha, 0 | \nu_\beta, t \rangle \,|^2 = Tr(\rho_\alpha(0) \cdot \rho_\beta(t)) \tag{16}$$

with $\rho_\alpha(0) = |\nu_\alpha\rangle \langle \nu_\alpha|$. So we can rewrite (16) using (15) as

$$P_{\alpha\to\beta} = \sum_{j,k} U_{\beta j}\, U^*_{\alpha j}\, U_{\alpha k}\, U^*_{\beta k}\, e^{-i\Delta_{jk}t} \ . \tag{17}$$

This shows that the oscillations are caused by the differences in the energies Δ_{jk}. As neutrino masses are very small (which was shown by experiments), neutrinos are extremely relativistic particles, so their energy is approximately their momentum. This implies (expanding the energies to order $\frac{m_i^2}{E^2}$):

$$\Delta_{ij} \approx \frac{m_i^2 - m_j^2}{2E} \tag{18}$$

with $E = \frac{1}{3}(E_1 + E_2 + E_3)$. So the oscillations arise due to mass differences of the neutrinos. As oscillations have been observed by several experiments in the last decades, it is highly improbable that more than one neutrino has zero mass.

Taking matter effects into account, we have to add an additional term to our vacuum Hamiltonian. As matter is dominated by electrons, mainly electron neutrinos will interact with it in weak charged-current interactions. In flavour basis, we therefore get

$$H_{int} \approx \sqrt{2}\, G_F\, n_e \begin{pmatrix} 1 & 0 & 0 \\ 0 & 0 & 0 \\ 0 & 0 & 0 \end{pmatrix} \ . \tag{19}$$

These interactions are influenced by the electron density n_e in that specific matter and by the Fermi coupling constant $G_F = \frac{\sqrt{2}g^2}{8m_W^2}$ with the electroweak coupling constant g and the mass m_W of the W-boson. This gives the effective Hamiltonian in mass basis:

$$H_{eff} = H_{vac} + U^\dagger H_{int}\, U \ . \tag{20}$$

Inserting this Hamiltonian into (13) gives the solution for propagation in matter.

2.2 Oscillations with Decoherence

As a next step, we want to consider oscillations in matter that are affected by decoherence. Our starting point is again equation (2). This equation describes the time evolution of a neutrino system without decoherence. To include decoherence effects, we have to add an extra term that models them, which we call $\mathcal{D}[\rho]$. We now consider the neutrino system as an open system coupled to the environment. This coupling is represented by an additional term in the time evolution equation (2) which can be written down (following the formalism in [24]) as:

$$\partial_t \rho(t) = -i[H, \rho(t)] - \mathcal{D}[\rho](t) \ . \tag{21}$$

This equation together with a certain choice for $\mathcal{D}[\rho](t)$ (see below) is called the Lindblad Master equation and allows transition from a pure to a mixed state. It is the most general time evolution equation that neglects memory effects, which are effects that happen due to prior states of the neutrino system. They happen on much shorter timescales than oscillations, thus they are unimportant for our purposes. Before imposing additional physical conditions on the Lindblad Master equation, we want to choose a suitable basis for our system. As we include matter effects according to (20), the effective Hamiltonian is no more diagonal. Nevertheless, this Hamiltonian is still hermitian and therefore we can diagonalise it again and work in the basis, where it is diagonal. We will call this basis the effective mass basis and denote objects in this basis with $\tilde{m}$ in the index. The effective Hamiltonian is constant in time, thus also the transformation into the effective mass basis is constant in time and commutes with time derivatives. This gives the Lindblad Master equation in the chosen effective mass basis:

$$\partial_t \rho_{\tilde{m}}(t) = -i[H_{\tilde{m}}, \rho_{\tilde{m}}(t)] - \mathcal{D}[\rho_{\tilde{m}}](t) \ . \tag{22}$$

Equations of this form can also be seen as generators of a quantum dynamical semigroup γ_t with

$$\gamma_t : \rho_{\tilde{m}} \mapsto \rho_{\tilde{m}}(t) \tag{23}$$

for $t \geq 0$ and with group composition law

$$\gamma_t \circ \gamma_s = \gamma_{t+s} \tag{24}$$

for $t, s \geq 0$ (for detailed information see for example [25] or [26]). We continue by imposing a few physical conditions on our neutrino system. First of all, we want to have conserved probability for any initial state. This is equivalent to requiring a constant trace of the density matrix $\rho_{\tilde{m}}$. In addition to that, we also expect the individual probabilities for the different neutrino states to be positive or zero for all times in future. In a closed system, this is equivalent to positivity. As we treat an open system coupled to the environment, we even need complete positivity. This ensures that interactions within

our system and with the environment keep the probabilities for the different states non-negative. These two conditions fix the form of $\mathcal{D}[\rho_{\tilde{m}}](t)$ to

$$\mathcal{D}[\rho_{\tilde{m}}](t) = \sum_{n=1}^{dim(\mathcal{H})^2-1} (\{\rho_{\tilde{m}}(t), D_n^\dagger D_n\} - 2\, D_n\, \rho_{\tilde{m}}(t)\, D_n^\dagger) \ . \tag{25}$$

In this equation, $\{.,.\}$ denotes the anticommutator. The sum goes from one to the dimension of the Hilbert space of the system of interest squared minus one. For our three-flavour picture, it goes from one to eight, so we get eight operators D_n. These operators form by construction an orthonormal basis set in the neutrino mass basis with

$$\sum_j D_n^\dagger D_n < \infty \ . \tag{26}$$

We also expect the von-Neumann entropy

$$S[\rho_{\tilde{m}}](t) = Tr[\rho_{\tilde{m}}(t) \cdot ln(\rho_{\tilde{m}}(t))] \tag{27}$$

to permanently increase with time. This can be modeled by assuming the D_ns to be hermitian (see [27]). A last condition which we impose onto our system is energy conservation. This is a strong constraint and a priori not justified, as we coupled our system to the environment. On the physical side, energy loss is characteristic for dissipation, while energy conservation is characteristic for decoherence processes. As we expect decoherence to occur faster than dissipation, we include energy conservation into our set of physical conditions. On the technical side, without conserved energy our system would have 36 new parameters (which are far too many unknowns for a first investigation of decoherence effects), with conserved energy we only get three new parameters for the three flavour case. Energy conservation, which can be expressed as

$$\partial_t Tr[H_{\tilde{m}}\, \rho_{\tilde{m}}(t)] = 0 \ , \tag{28}$$

can be achieved by requiring $H_{\tilde{m}}$ to commute with the D_n, that is

$$[H_{\tilde{m}}, D_n] = 0 \ . \tag{29}$$

This means that Hamiltonian and D_ns can be diagonalised simultaneously. We assume that this happens in the effective mass basis and therefore the D_ns in this basis are given by

$$D_n = diag\{d_{n1}, d_{n2}, d_{n3}\}_{\tilde{m}} = D_n^\dagger \ . \tag{30}$$

We will now sketch the derivation of the solution for (21) using the above discussed decoherence term and working in the effective mass basis following [15]. With the specific form (30) of D_n and its hermiticity, the anticommutator in (25) becomes

$$\Big(\{\rho_{\tilde{m}}(t), D_n^\dagger D_n\}\Big)_{ij} = (d_{ni}^2 + d_{nj}^2) \cdot (\rho_{\tilde{m}})_{ij}(t) \ . \tag{31}$$

The other part of the decoherence term gets

$$\left(-2\, D_n\, \rho_{\tilde{m}}(t)\, D_n^\dagger\right)_{ij} = -2\, d_{ni}\, d_{nj} \cdot (\rho_{\tilde{m}})_{ij}(t) \tag{32}$$

and thus the entire decoherence term in the Lindblad Master equation reads

$$(\mathcal{D}[\rho_{\tilde{m}}](t))_{ij} = \Gamma_{ij} \cdot (\rho_{\tilde{m}})_{ij}(t) \cdot (1 - \delta_{ij}) \tag{33}$$

with $\Gamma_{ij} := \sum_{n=1}^{8} (d_{ni} - d_{nj})^2$. The decoherence is now encoded in the six parameters $\{\Gamma_{ij}\}_{i,j\in\{1,2,3\}, i\neq j}$. From the definition of the Γ_{ij} it is immediately apparent that they are symmetric in i and j, so decoherence is described by only three parameters, Γ_{21}, Γ_{31} and Γ_{32}. They are still not three independent parameters, but due to their definition via the d_{ni}, two can be picked completely free and the third one is then only an angular degree of freedom. This can be seen by setting one Γ_{ij} to zero. Then the two remaining Γs have the same value according to their definition. This dependency can be expressed by using as degrees of freedom Γ_{21}, Γ_{31}, and a decoherence angle Θ and leads to

$$\Gamma_{32} := \Gamma_{31} + \Gamma_{21} \cos^2(\Theta) - \cos(\Theta) \sqrt{\Gamma_{21}\,(4\,\Gamma_{31} - \Gamma_{21}\,(1 - \cos(\Theta))}\ . \tag{34}$$

Now we want to use this form of the decoherence term to find a solution for (22). Evaluating the commutator in this equation and then subtracting (33) from it, we see that, compared to section 2,

$$-\,i\Delta_{ij} \quad \longrightarrow \quad -i(\Delta_{\tilde{m}})_{ij} - \Gamma_{ij}\ . \tag{35}$$

This can also be shown by repeating the derivation shown in section 2 with the Lindblad Master equation in effective mass basis. This will give an equation similar to (12), but including also the coefficient matrix (which is diagonal as well) of the D_n expanded in terms of the Gell-Mann matrices. As we would expect from (35), the final solution then is

$$\rho_{\tilde{m}}(t) = \begin{pmatrix} (\rho_{\tilde{m}})_{11}(0) & (\rho_{\tilde{m}})^*_{21}(0)\, e^{i\Delta_{21}t - \Gamma_{21}t} & (\rho_{\tilde{m}})^*_{31}(0)\, e^{i\Delta_{31}t - \Gamma_{31}t} \\ (\rho_{\tilde{m}})_{21}(0)\, e^{-i\Delta_{21}t - \Gamma_{21}t} & (\rho_{\tilde{m}})_{22}(0) & (\rho_{\tilde{m}})^*_{32}(0)\, e^{i\Delta_{32}t - \Gamma_{32}t} \\ (\rho_{\tilde{m}})_{31}(0)\, e^{-i\Delta_{31}t - \Gamma_{31}t} & (\rho_{\tilde{m}})_{32}(0)\, e^{-i\Delta_{32}t - \Gamma_{32}t} & (\rho_{\tilde{m}})_{33}(0) \end{pmatrix}\ . \tag{36}$$

Transition probabilities can be calculated analogously to (17) by using the unitary transformation which transforms into the effective mass basis and the assignment (35).

3 The ORCA Detector

In this section, we will take a closer look on ORCA, the detector for which we perform the decoherence analysis. Before going into technical detail, we first sketch how neutrino detection is feasible.

3.1 Neutrino Detection

As already mentioned above, neutrinos only interact in weak interactions. Therefore it is not possible to detect them directly. So a neutrino detector has to focus on measuring secondary particles created by such a weak neutrino interaction. During a weak interaction, two interacting particles exchange a boson, either a $W^{\pm}$ or a Z^0 boson. Depending on the kind of boson that is exchanged, two different current interactions can be distinguished: the CC interaction is transmission of charged current ($W^{\pm}$ boson), while the NC interaction is transmission of neutral current (Z^0 boson). In CC interactions, the neutrino is converted into a lepton with the same flavour the neutrino had and a hadronic shower is created. NC interactions result in the conservation of the neutrino and also a hadronic shower.

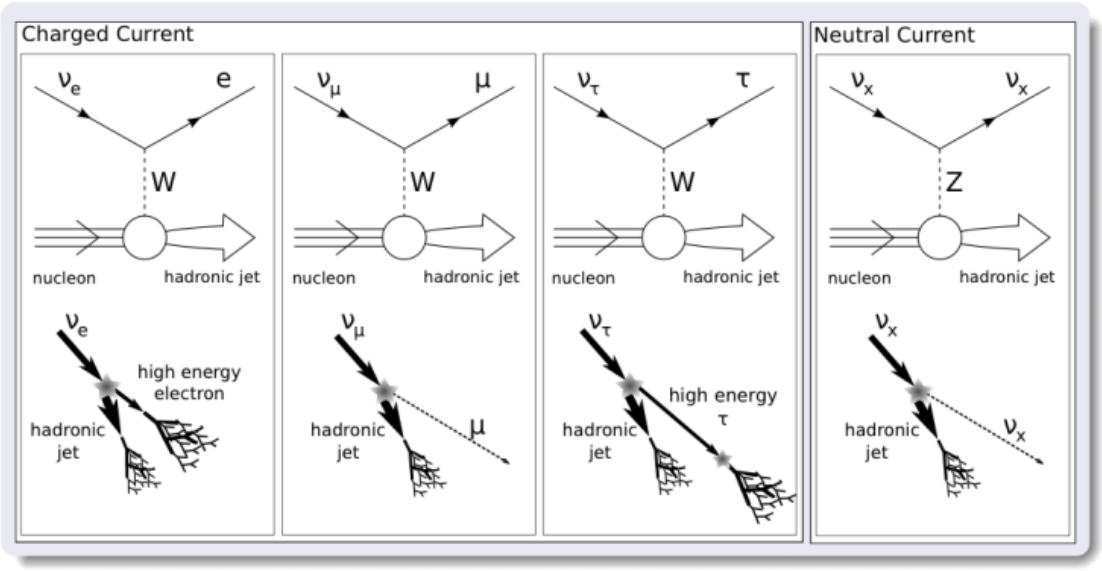

Figure 1: Interaction channels of neutrinos with matter. (credit: J. Tiffenberg, NUSKY11)

For a detector, shower-like and track-like light emission is visible. Different kinds of shower-like events are very difficult to distinguish. Thus NC actions look the same, no matter which neutrino flavour took part in it. In contrary, for CC actions the original neutrino properties can be determined up to a certain degree of probability. As matter

consists of electrons, in CC interactions created electrons have a short mean free path and end up in an additional shower which creates multiple particles. Muons have a large mean free path and will therefore pass through the detector leaving a track. Tau leptons have a very short mean free path and form two showers, which are separated at the relevant GeV energies by a much shorter distance than the detector can measure. All charged particles propagating through matter polarise the atoms along their path and therefore create an electromagnetic wave. Neutrinos are highly relativistic particles, which means they have very high momenta. Therefore also many particles, which are created by the weak interaction, have high momenta due to momentum conservation. This results in a particle's velocity greater than the speed of light in matter. So a charged particle might be faster than the electromagnetic wave created by polarisation of the medium. Then the waves created in different atoms cannot interfere destructively, but form a radiation cone. This radiation can then be detected and is called Cherenkov radiation. From this behaviour arises the classification of two main event topologies: track-like events on the one hand, which contain CC muon interactions, and shower-like events on the other hand, which contain all other interaction channels.

3.2 KM3NeT - Cubic Kilometre Neutrino Telescope

The ORCA detector, which is short for Oscillation Research with Cosmics in the Abyss, is part of KM3NeT, short for Cubic Kilometre Neutrino Telescope, which is being built in the Mediterranean Sea. ORCA consists of one building block (see Figure 2) and is located in the deep-sea, about $40km$ offshore from Toulon in France. Aside from ORCA, the other two building blocks which are to be deployed offshore from Sicily form ARCA (short for Astroparticle Research with Cosmics in the Abyss). While ORCA's specifications are optimised for evaluating oscillation parameters of neutrinos, ARCA's main goal is to find sources of high-energetic neutrinos in the Galaxy. The building blocks are similar and consist of the same parts, only the spacing between the single detectors in each block is different for ORCA and ARCA. For investigating decoherence in oscillations, the natural choice is to work with data collected by ORCA. Thus our analysis will focus on ORCA.

3.3 Photomultiplier Tube

A photomultiplier tube (PMT) is a detector to measure photons. It can detect single photons, but therefore works best with as few background photons as possible. As KM3NeT is located at the bottom of the deep-sea, no light from the sun reaches the detector. Thus PMTs are a very good choice to detect photons from the Cherenkov radiation of particles propagating through water near the detector. In this section, we briefly sketch the functionality of a PMT (see also Figure 3 for visualisation): An incident photon hits the photocathode and ejects an electron from it. Inside the tube, a

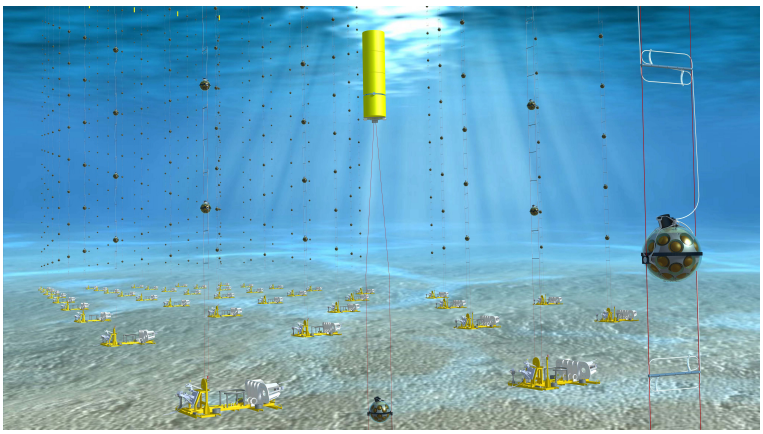

Figure 2: A building block of KM3NeT (Artist's impression). (credits: Edward Berbee/Nikhef and KM3NeT)

high voltage is applied, such that a large attracting force towards the other end of the tube acts on the electron. So the electron is accelerated quickly. After passing through a focusing electrode, it hits a first dynode. This process frees some new electrons which are accelerated again and hit a second dynode after short propagation time. Each electron frees a bunch of new ones and the process continues. After certain dynodes, a high current of electrons has been created by the incident photon(s). This high current is visible very well and converted into an electrical signal at the end of the tube.

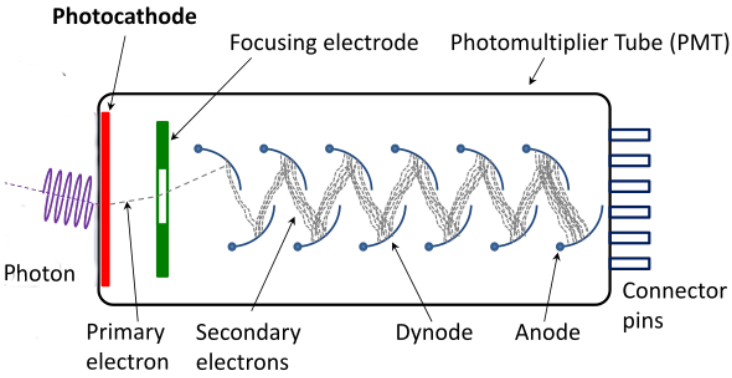

Figure 3: A photomultiplier tube. (from Wikimedia Commons)

3.4 ORCA - Oscillation Research with Cosmics in the Abyss

ORCA is formed by 115 strings. These strings are fixed on the sea floor with one end, while on the other end a buoy arranges each string such that it points vertically upwards.

Each string consists of 18 digital optical modules (DOMs, see Figure 4). The DOMs are pressure-resistant glass spheres containing 31 PMTs each. These PMTs emit a signal, if they detect a photon. The spacing of the single strings is about $20m$ horizontally. The DOMs are separated about $9m$ vertically and start about $40m$ above sea floor. These distances make it possible to address neutrino energies in the GeV range. The first strings have already been deployed. According to schedule, ORCA should be completed by 2020.

Figure 4: A digital optical module (DOM) used for KM3NeT. (credits: KM3NeT)

The PMTs in the DOMs are distributed in five rings with six PMTs each. One additional multiplier tube is at the bottom of the DOM, so it contains in total 19 PMTs in the lower and 12 in the upper hemisphere. The PMTs have a photo-cathode diameter of at least $72mm$ and a length of $122mm$. They consist of a ten stage dynode. High voltage applied to it creates an amplification of $3 \cdot 10^6$. A reflector ring around the face of each PMT increases the photon collection efficiency of each PMT by about one third. To keep up optical contact between the PMT and the glass, the cavity inbetween is filled with an optical gel. In addition to the 31 PMTs, each DOM also contains sensors

permanently reporting its orientation and direction. All sensors and PMTs of one DOM consume about 7 W together.

All data collected by the detector (with a trigger of approximately 0.3 photo-electrons) is transferred to shore with a bandwidth of $1\,Gb/s$ per DOM. There, different filters on multiple levels are applied to drop events which were not caused by neutrinos. These backgrounds arise for example in atmospheric muons, bioluminescence caused by organisms in the deep sea, or $40K$ decays (that create electrons, anti electron-neutrinos and photons among other particles). After that, several algorithms separate track- and shower-like event topologies from which we can infer on the original neutrino, its approximate energy and direction.

3.5 Limits on the precision

Uncertainties on the reconstructed neutrino come from many different factors. To start with, ORCA cannot distinguish neutrinos and antineutrinos. However, as from GeV energies upwards the crossections of neutrinos and antineutrinos differ by a factor of two, one can include this into the reconstruction process. Uncertainties in the oscillation parameters of the neutrino and also in the atmospheric spectra, neutrino flux and earth matter density profile prevent us from calculating the exact amount of neutrinos reaching the detector. Also during weak interactions information is lost, as the leptons created in this interactions do not propagate in exactly the same direction as the neutrino did before. In addition, fluctuations in the development of particle cascades and in the production and propagation of their Cherenkov radiation exist. Furthermore, the detector has only limited efficiency and does not detect all photons. Finally, the filter and reconstruction algorithms do not give perfect results. All these sources of errors and limits on the precision lead to a smearing of the output of the detector. We will see later that this smearing has high impact on our analysis. More information on limits on the precision and a detailed analysis of uncertainties for charged current events can be found in [28].

4 Software and Setup

In this section we introduce our simulation tools. We start by illustrating the model we used for the earth. Then we explain OscProb, which computes oscillation probabilities of neutrinos. This program is included in paramNMH, a tool to transform the incident neutrinos into event rates adapted to ORCA. Finally we document the considered oscillation parameters and discuss the investigated parameter space for the decoherence parameters.

4.1 Model for Earth: PREM

Atmospheric muons are a big issue for neutrino astronomy. As one cannot hardly distinguish whether a downgoing muon was created by a neutrino interaction or by a reaction of the cosmic background radiation with the atmosphere, such downgoing muons are no reliable source for neutrino measurements. Therefore neutrino detectors measure particles that propagate through the earth. Neutrinos have a much higher mean free path than muons. So, while muons cannot penetrate the earth, almost all neutrinos can at the relevant GeV energies. According to the above derived formulae for oscillations, matter affects the neutrino oscillations, so we need to know the properties of the earth and its density at different radii. In addition to that, we also need to know the kind of matter dominating each layer in order to be able to calculate the neutrino interaction probability. To get this information, we use the Preliminary Reference Earth Model (PREM). This model gives different physical quantities of the earth, like its density, with respect to the radius. It was developed in 1981 by geophysicists (see [29]) and is sufficient for our purpose. We interpolate it using 44 layers, which is an appropriate compromise between accuracy and computation time. The difference of the results compared to these using a more detailed interpolation is negligible. In Figure 5 this 44 layer model is visualised and the exact values are given in the Appendix, see 8.

4.2 Calculating neutrino oscillation probabilities: OscProb

OscProb is a set of classes to compute exact neutrino oscillation probabilities for different scenarios written in C++ by João A. B. Coelho (see [30]). It is based on a three flavour model and uses the CERN data analysis framework ROOT (see [31]). The library supports the following setups:

- Calculation of standard oscillation probabilities according to the procedure in section 2
- Calculation of oscillation probabilities including any number of sterile neutrinos
- Calculation of oscillation probabilities including non-standard interactions

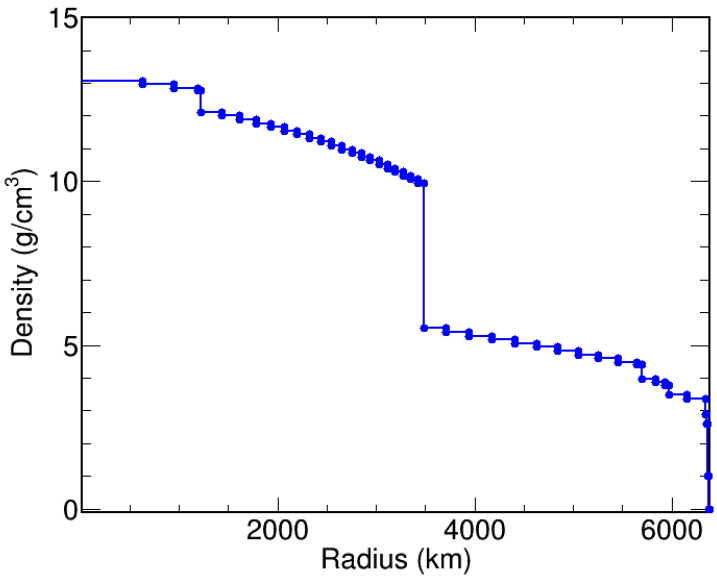

Figure 5: The 44 layer PREM with the Earth matter density and the radial distance to the centre of the Earth.

- Calculation of oscillation probabilities including the decoherence model introduced in section 2

All these oscillations can be evaluated in vacuum or matter. For the matter case OscProb comes along with the PREM and splits the calculation for the oscillation probabilities into single layers of constant density. Also a visualisation of the result in form of a histogram is implemented among other features.

4.3 Event rates for ORCA: paramNMH

paramNMH is a software package that simulates the detector response to an incident neutrino flux for ORCA. It uses OscProb to calculate neutrino oscillation probabilities and the Honda atmospheric neutrino flux model (see [32]) as parametrisation for the original incident neutrino flux. The outcome is the number of events that are reconstructed for a certain energy E^{rec} and a certain zenith angle Θ^{rec}. The event number is different for tracks and showers. It is calculated via

$$N_\alpha(\Theta^{rec}, E^{rec}) = \int dE\, d\Theta \sum_i P^{ID}_{i\alpha}(E)\, P^{rec}_{i\alpha}(\Theta^{rec}, E^{rec}|\Theta, E)\, M^{eff}_i(\Theta, E)\, N^{int}_i(\Theta, E)\ . \tag{37}$$

Here, the index α denotes the classification of an event as track-like or shower-like. The index i in the sum goes over all different neutrino flavours and (anti-)neutrinos. In the

formula appears the term $P_{i\alpha}^{ID}(E)$ that gives the probability for a neutrino i of energy E to be classified as an event α. Another contribution is $P_{i\alpha}^{rec}(\Theta^{rec}, E^{rec}|\Theta, E)$ which models the detector response function, that is the probability for an event with energy E and zenith angle Θ to be reconstructed with the energy E^{rec} and the zenith angle Θ^{rec}. $N_i^{int}(\Theta, E)$ denotes the number of interacting neutrinos per unit mass of seawater. This quantity can be calculated using the (unoscillated) atmospheric neutrino flux $\Phi_j(\Theta, E)$, the oscillation probability of neutrino j oscillating into neutrino i, $P_{ji}^{osc}(\Theta, E)$, the crossection $\sigma_i(E)$ of neutrino i, the mass $m_{nucleon}$ of the nucleons in water and the live time Δt:

$$N_i^{int}(\Theta, E) = \frac{\sigma_i(E)\,\Delta t}{m_{nucleon}} \sum_j \Phi_j(\Theta, E)\, P_{ji}^{osc}(\Theta, E)\ . \tag{38}$$

The last quantity left in (37) is the effective mass $M_i^{eff}(\Theta, E)$. This gives the mass of water contained in an equivalent detector with 100% detection efficiency and can be calculated using

$$M_i^{eff}(\Theta, E) = \rho_{water}\, V_{gen}\, \frac{N_i^{sel}(\Theta, E)}{N_i^{int}(\Theta, E)}\ . \tag{39}$$

Here, ρ_{water} is the density of seawater, V_{gen} the volume where the events are generated and $N_i^{sel}(\Theta, E)$ the number of selected events.
paramNMH evaluates the number of events for tracks and showers for a given reconstructed energy and zenith angle range according to equation (37). As parameters it uses the specifications of ORCA, the Honda neutrino flux model and oscillation probabilities provided by OscProb.

4.4 Considered oscillation parameters

As already mentioned, a set of specifications for ORCA is already implemented in paramNMH. Earth was modeled according to the PREM with 44 layers. The oscillation parameters were chosen according to the most recent parameters in [12] (except for Θ_{32}, which fluctuates somewhere between 40° and 50° with each new measurement). The values are from January 2018 and can be seen in Table 1.

Parameter	Unit	normal ordering	inverted ordering
Δm_{21}^2	$10^{-5}\,eV^2$	7.40	7.40
Δm_{32}^2	$10^{-3}\,eV^2$	2.420	2.465
Θ_{21}	deg	33.62	33.62
Θ_{31}	deg	8.54	8.58
Θ_{32}	deg	45.0	45.0
δ_{CP}	deg	234	278

Table 1: Oscillation parameters used in our studies. Values taken from [12].

4.5 Investigated parameter space for the decoherence parameters

As outlined in the theory part (see section 2.2), using our approach we are left with three decoherence parameters Γ_{21}, Γ_{31} and Γ_{32}. In order to be able to make statements for the general case, we use three limiting cases. In each of the cases, we set one of the decoherence parameters to zero. The other two are then equal to each other, which follows directly from (34). So we get one effective decoherence parameter for each limiting case. These limits give the most conservative results for the entire parameter space of the three Γ_{ij}, which is shown in detail in Appendix B of [21]. The specific limits are:

Limit	Γ_{21}	Γ_{31}	Γ_{32}
atmospheric limit (Alim)	0	γ	γ
solar limit 1 (Slim1)	γ	γ	0
solar limit 2 (Slim2)	γ	0	γ

For each limit, experimental data of other neutrino telescopes has already been analysed and upper bounds on the decoherence parameter γ have been set: The data has been compared to theoretical expectations given with and without decoherence and the γ value has been determined that can be excluded on a 95% confidence level. This means that a decoherence parameter larger than the set upper bound can be excluded with a probability of 95% or more with the given experimental data (SK [17], MINOS [33], KamLAND [34], IceCube / DeepCore [21]). For our analysis, we used the lowest existing upper bounds as starting point. Furthermore we tested different energy dependencies of γ. In detail, we analysed the five cases of γ being independent of energy, or dependent on energy in a power law with exponent $\in \{\pm 1, \pm 2\}$, that is in general $\gamma = \gamma_0 \left(\frac{E}{GeV}\right)^n$ with $n \in \{0, \pm 1, \pm 2\}$. Aside from the limit, the bounds also depend on the neutrino mass ordering. The detailed starting parameters can be extracted from Table 2.

NO	$n = -2$	$n = -1$	$n = 0$	$n = 1$	$n = 2$
Alim	$4.3 \cdot 10^{-20}$	$2.5 \cdot 10^{-22}$	$\mathbf{4.0 \cdot 10^{-24}}$	$1.0 \cdot 10^{-27}$	$1.0 \cdot 10^{-31}$
Slim1	$1.2 \cdot 10^{-20}$	$2.5 \cdot 10^{-22}$	$1.3 \cdot 10^{-24}$	$3.5 \cdot 10^{-28}$	$1.9 \cdot 10^{-32}$
Slim2	$7.5 \cdot 10^{-21}$	$3.7 \cdot 10^{-24}$	$9.7 \cdot 10^{-25}$	$2.4 \cdot 10^{-28}$	$9.0 \cdot 10^{-33}$
IO					
Alim	$1.4 \cdot 10^{-20}$	$2.5 \cdot 10^{-22}$	$1.3 \cdot 10^{-24}$	$3.5 \cdot 10^{-28}$	$1.9 \cdot 10^{-32}$
Slim1	$8.3 \cdot 10^{-21}$	$2.5 \cdot 10^{-22}$	$9.8 \cdot 10^{-25}$	$2.4 \cdot 10^{-28}$	$9.0 \cdot 10^{-33}$
Slim2	$5.0 \cdot 10^{-20}$	$3.7 \cdot 10^{-24}$	$4.1 \cdot 10^{-24}$	$1.0 \cdot 10^{-27}$	$1.0 \cdot 10^{-31}$

Table 2: Upper limits for the decoherence parameter on 95% CL from data collected by SK [17], MINOS [33], KamLAND [34] and IceCube/DeepCore [21]. The bold value will be used as example in section 5.1.

5 Sensitivity of ORCA to the most recent lowest decoherence bounds

In the next two sections we present our results and discuss them. In this section we start by visualising the impact of the detector on the results. Then we give the sensitivity of ORCA to decoherence using the lowest bounds previously found by other experiments and summarised in Table 2.

5.1 From flux to asymmetries

5.1.1 Flavour topologies

We start with analysing the loss of information and the flow of data given by the Honda neutrino flux through the detector (modeled by OscProb and paramNMH). For this analysis we focus on the atmospheric limit in normal ordering (NO) with an energy independent decoherence parameter. It can be generalised to the other cases. In Figures 6 and 7 are shown the event rates of neutrinos separately for electron, muon and tau neutrinos, that are measured by the detector within three years. The first figure corresponds to no decoherence, the second one to the atmospheric limit for decoherence, thus using $\gamma = 4.0 \cdot 10^{-24}$ (see Table 2). For the analysis a binning of 100×100 was used. From the figures it is apparent that the event number of the different neutrino types differs reasonably. While detected electron neutrinos mainly carry energies between 4 GeV and 10 GeV and arrive at a zenith angle close to 90° (horizon), detected tau neutrinos, which are almost all generated by oscillations, are dominant in the sector between 20 GeV and 30 GeV for a zenith angle close to 180° (up-going) and form a broad band up to a zenith angle of approximately 105°, where their number and energy decreases. Below 3 GeV no tau neutrinos arrive at the detector, as the production energy threshold for tau leptons is approximately 3 GeV. In the event number diagram of the muon neutrinos the oscillation pattern is more apparent. Clearly visible is the band, where some of the muon neutrinos oscillate into tau neutrinos between 20 GeV and 30 GeV for a zenith angle close to 180°. Decoherence does not change these structures. This is due to the relatively small distance the neutrinos have travelled until they reach the detector, as neutrinos at this energy are all atmospheric neutrinos. Nevertheless, decoherence effects are clearly measurable at these energies, as we will see later in this section. Before we are able to extract this information about measurability of decoherence, we have to take into account the limited precision of detector and the reconstruction algorithms, which was discussed in section 3.5. This leads to a substantial decrease of structure in the oscillograms. Exemplary, this is shown in Figures 8 for no decoherence and 9 for the decoherence case considered in Figure 7. The concentration of the distinct flavours at different positions in the diagrams is still clearly recognizable. While the structure of the tau and electron neutrinos is still approximately the same as before, as they do

not show subtle structures, the oscillatory structure prior observed in the oscillogram of the muon neutrinos now has completely vanished. The reason lies in the different event topologies of the neutrino flavours, which were introduced in section 3.1: On one side, an interaction of tau or electron neutrinos ends up in showers, which produce a lot of particles that can be detected and therefore the direction and energy of the original neutrino can be reconstructed fairly well. On the other side, an interaction of a muon neutrino produces a muon. Muons are minimal ionising particles according to Bethe-Bloch, which means that their energy loss while propagating through a medium is very low compared to other particles like electrons or tauons. Thus they form a long track and leave the detector. A consequence of that is loss of information, so it becomes much more difficult to reconstruct the energy of the muon and therefore also the energy of the original neutrino cannot be reconstructed with such a high precision as the energy of an electron or tau neutrino. This results in the complete loss of the oscillatory structure of muon neutrinos in the oscillogram. Considering the tau neutrino diagram, it is conspicuous that the reconstructed energy range of the neutrinos differs clearly from the original one. Before the detector, the above mentioned energy band started between 20 GeV and 30 GeV at zenith angle 180°. The reconstruction algorithms lower the energy associated to this band by roughly 10 GeV. Also the oscillatory structure, that gets smeared due to the detector, is located at lower energies than it originally was: Before detector reconstruction effects it was close to 8 GeV, afterwards it is lowered to approximately 5.5 GeV. So the reconstruction algorithm for tau neutrinos is not optimal concerning their original energies. This energy shift arises in the decay chain of the created tauon: When the tauon decays, it creates apart from an electron / muon / hadronic shower also one or two electron / muon neutrinos. These neutrinos carry some energy of the original tau neutrino out of the system, which cannot be measured. In Figure 10 the asymmetry between the case without decoherence and the above specified atmospheric limit is plotted. The asymmetry is a quantity to compare both cases and was calculated for each bin of the oscillogram using the following formula:

$$Asym := \frac{AL - ND}{\sqrt{ND}} \ , \tag{40}$$

where AL denotes the bin value of the atmospheric limit and ND the value of the case with no decoherence. In our case we see that the asymmetry is very small for electron neutrinos. There is one mentionable difference of more than 4 % at a reconstructed energy of about 7 GeV. Here, the atmospheric limit predicts more electron neutrinos coming from the center of the earth with a smaller cosine of the zenith angle than is the case without decoherence. But in exchange to that, it suggests less neutrinos at the same energy to come from a zenith angle of approximately 134°. For muon and tau neutrinos, the decoherence effect is clearly visible at energies around 25 GeV. Here the asymmetry is quite large at about 10 %. While the asymmetry for electron and muon neutrinos tends to vanish for higher energies, it increases for tau neutrinos and reaches

its maximum of more than 15 % in the oscillogram for the highest considered energy of 100 GeV. Thus decoherence effects may also be worth to be investigated by detectors covering higher energy ranges than ORCA, like ARCA.

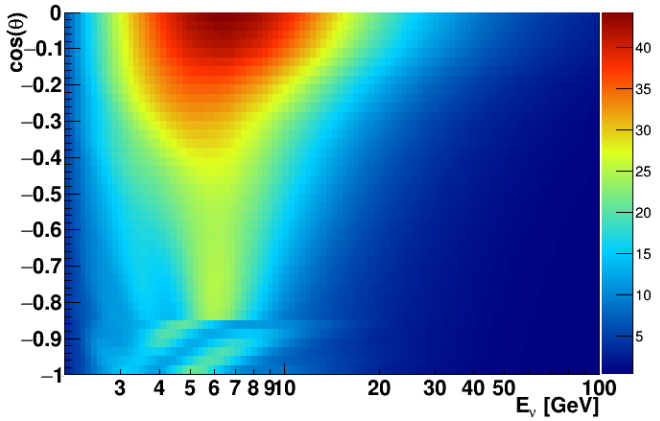

(a) Electron neutrinos

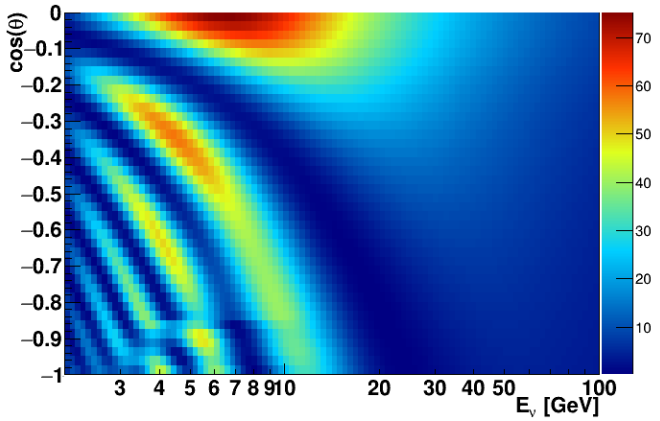

(b) Muon neutrinos

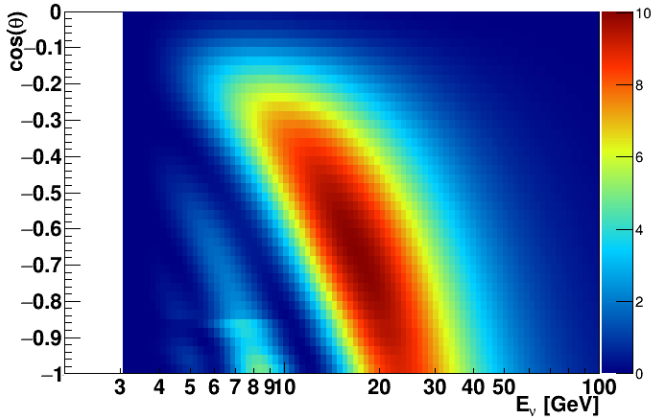

(c) Tau neutrinos

Figure 6: Number of detected events within three years for the different neutrino flavours for no decoherence and normal ordering. $\cos(\Theta)$ denotes the cosine of the zenith angle, E_ν the true energy of the neutrino.

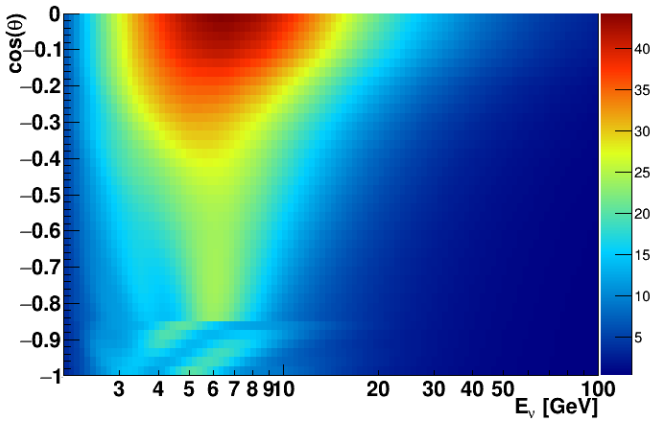

(a) Electron neutrinos

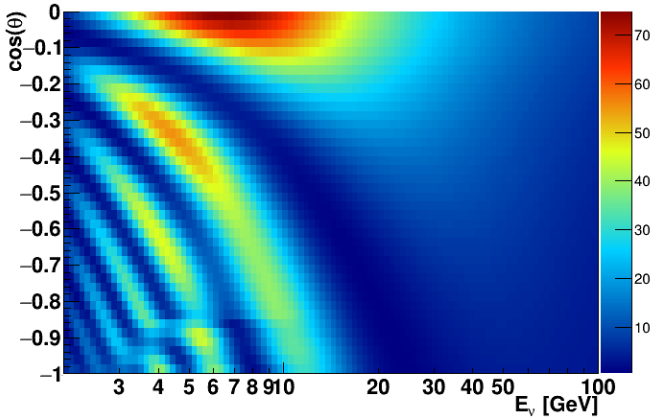

(b) Muon neutrinos

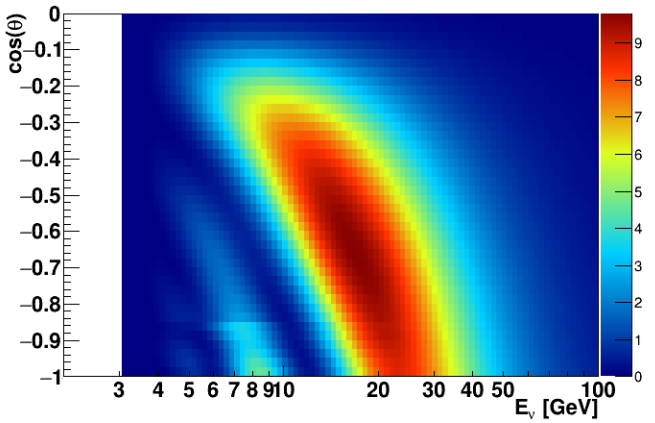

(c) Tau neutrinos

Figure 7: Number of detected events within three years for the different neutrino flavours for atmospheric limit, normal ordering, without energy dependence of γ (see Table 2). $\cos(\Theta)$ denotes the cosine of the zenith angle, E_ν the true energy of the neutrino.

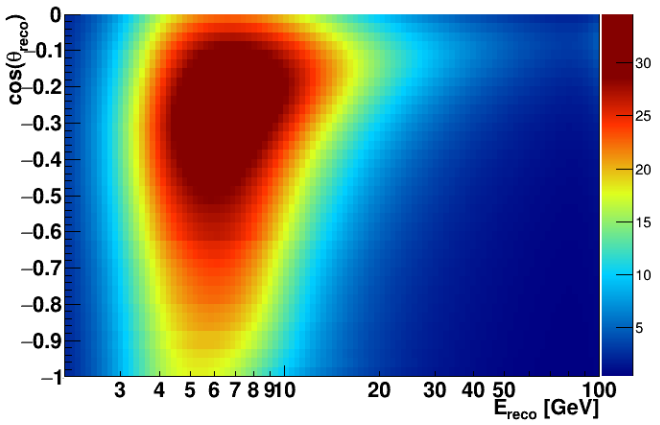

(a) Electron neutrinos

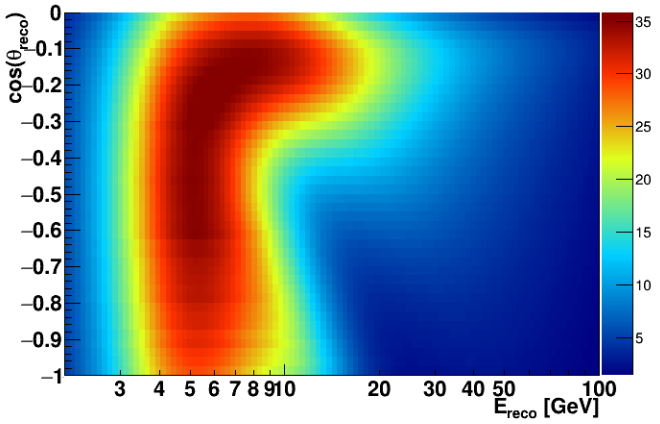

(b) Muon neutrinos

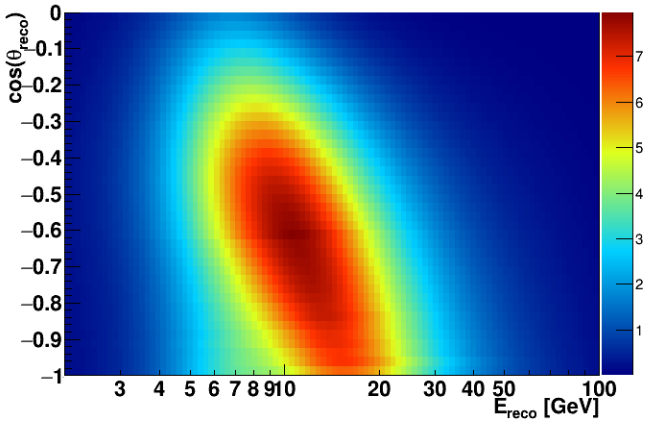

(c) Tau neutrinos

Figure 8: Number of detected events within three years for the different neutrino flavours without decoherence and for normal ordering. $\cos(\Theta_{reco})$ denotes the reconstructed cosine of the zenith angle, E_{reco} the reconstructed energy of the neutrino.

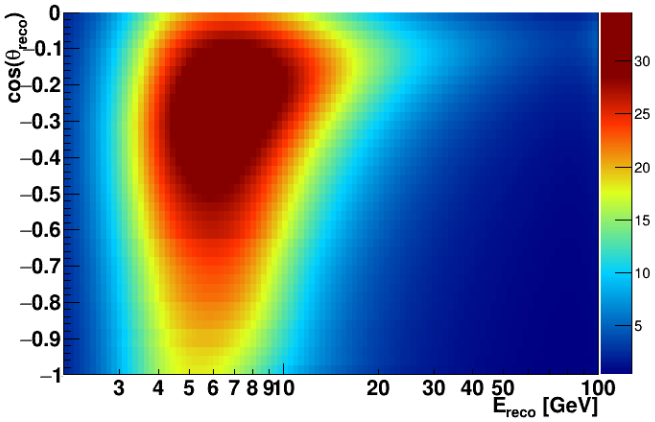

(a) Electron neutrinos

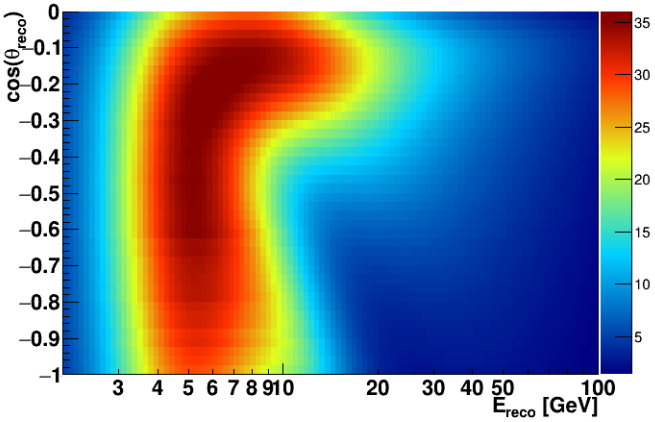

(b) Muon neutrinos

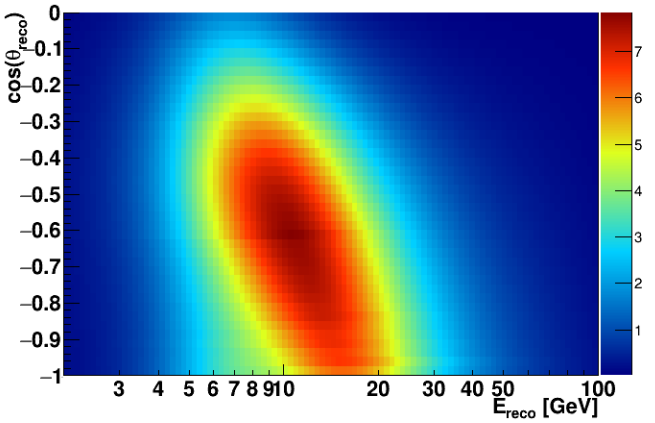

(c) Tau neutrinos

Figure 9: Number of detected events within three years for the different neutrino flavours for atmospheric limit, normal ordering, without energy dependence of γ (see Table 2). $\cos(\Theta_{reco})$ denotes the reconstructed cosine of the zenith angle, E_{reco} the reconstructed energy of the neutrino.

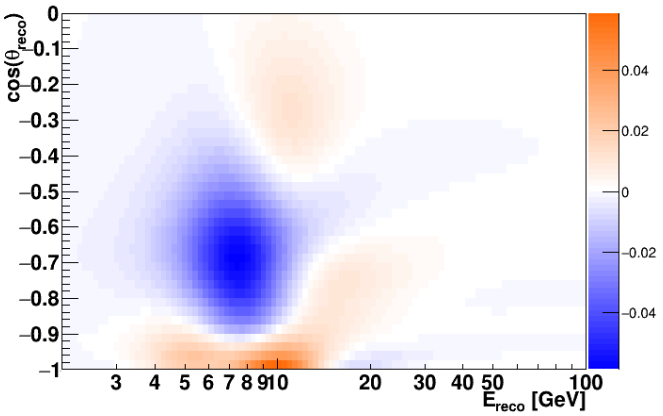

(a) Electron neutrinos

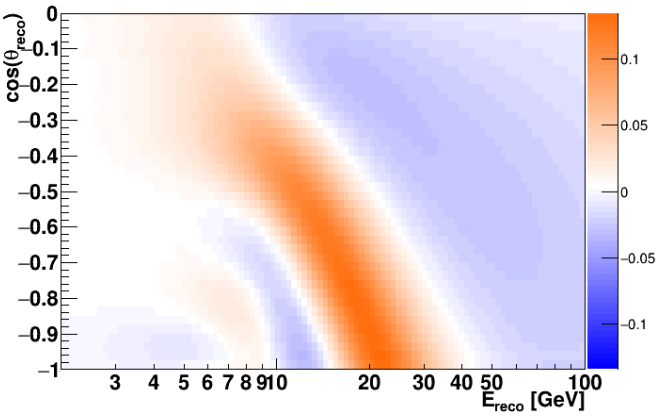

(b) Muon neutrinos

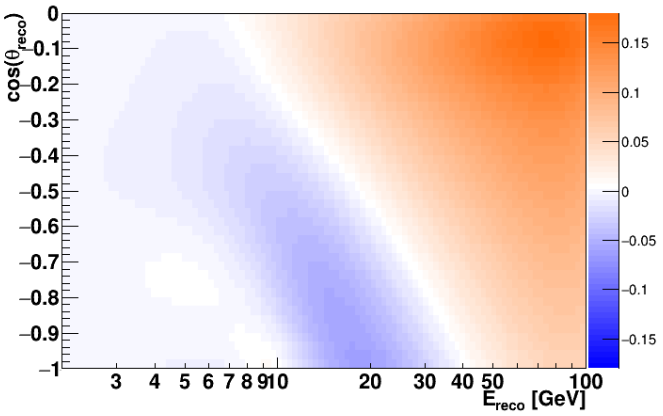

(c) Tau neutrinos

Figure 10: Asymmetries between the atmospheric limit (normal ordering, without energy dependence of γ, see Table 2) and no decoherence on the number of detected events within three years for the different neutrino flavours. $\cos(\Theta_{reco})$ denotes the reconstructed cosine of the zenith angle, E_{reco} the reconstructed energy of the neutrino.

5.1.2 Event topologies

Unfortunately ORCA cannot distinguish the three neutrino flavours very well, as was explained in section 3.1. Only a separation in track-like and shower-like events is possible, which leads to an additional loss of information. In Figure 11 the event rates for these two topologies are visualised for no decoherence, in Figure 12 they were calculated with decoherence in the same atmospheric limit that was considered in section 5.1.1. The behaviour of the secondary particles created by the different neutrino types can be recognized very well. The shower-like events mainly arise from electron and tau neutrinos. Therefore the pattern of the shower-like events is a combination of the patterns obtained for electron and tau neutrinos (compare for example Figure 8 to Figure 11). The band created by the tau neutrinos is not directly apparent any more in the shower-like event diagram. This is due to the small amount of tau neutrinos being detected compared to the number of electron neutrinos in the same time interval. The underlying reason of that is the difference in the crossections for charged current tauon and electron / muon reactions, where the first one is much smaller than the latter two due to the large mass of the tauon. The asymmetry plots are shown in Figure 13. For the considered case, it is clearly recognizable and in some parts of the oscillogram even larger than 8 %. Such asymmetry plots form the first central result of our project, as they show, for which cases we are able to find new information on decoherence using ORCA. Thus we calculated the asymmetries for all cases named in section 4.5. These oscillograms will be discussed in the next section.

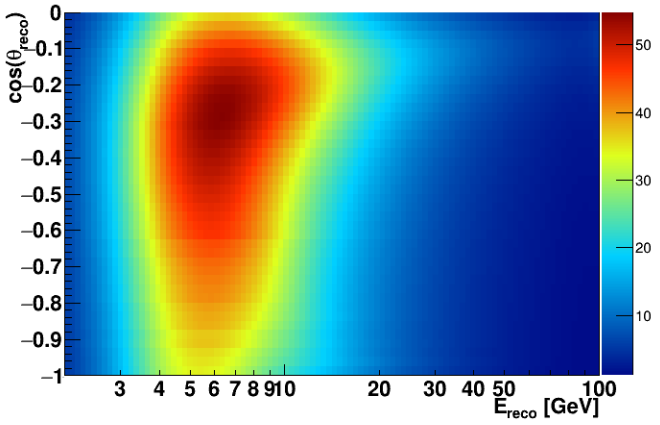

(a) Shower-like events

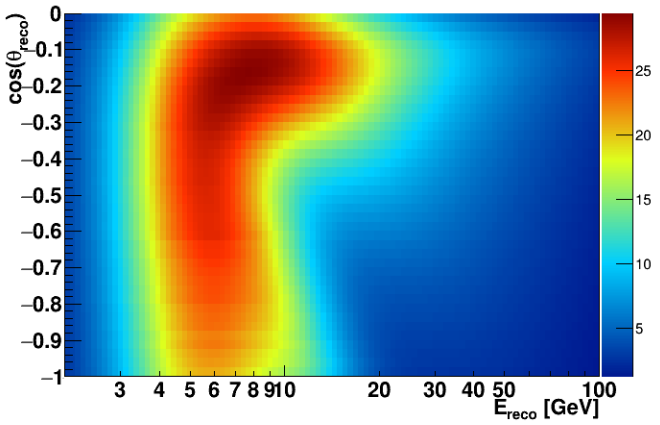

(b) Track-like events

Figure 11: Number of detected events within three years for the different event topologies without decoherence for normal ordering. $\cos(\Theta_{reco})$ denotes the reconstructed cosine of the zenith angle, E_{reco} the reconstructed energy of the neutrino.

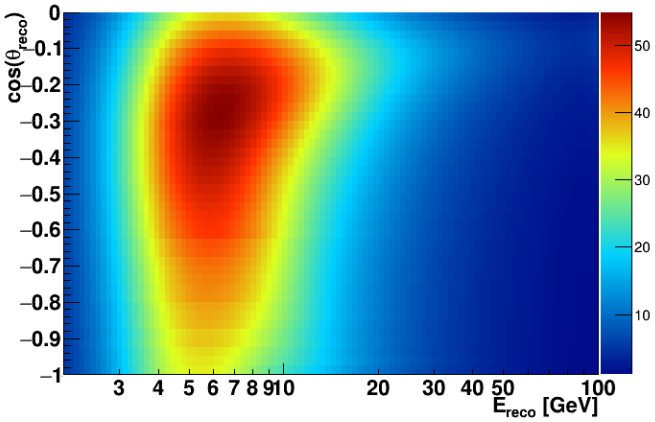

(a) Shower-like events

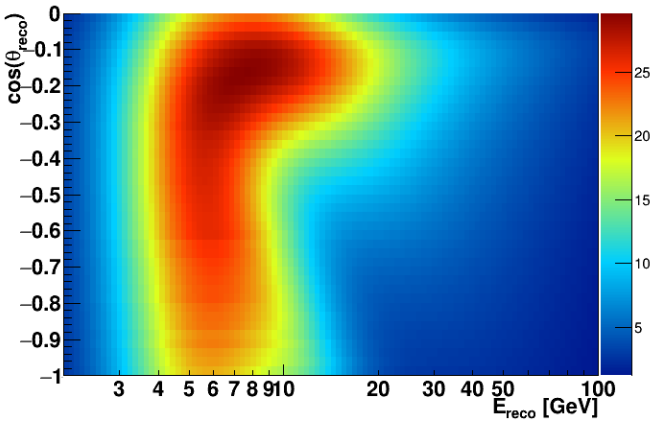

(b) Track-like events

Figure 12: Number of detected events within three years for the different event topologies for atmospheric limit, normal ordering, without energy dependence of γ (see Table 2). $\cos(\Theta_{reco})$ denotes the reconstructed cosine of the zenith angle, E_{reco} the reconstructed energy of the neutrino.

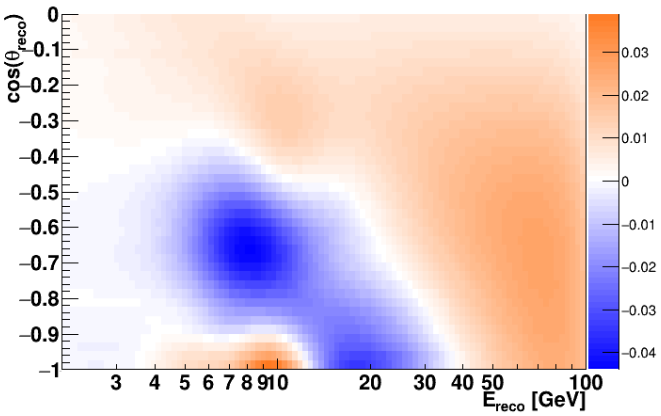

(a) Shower-like events

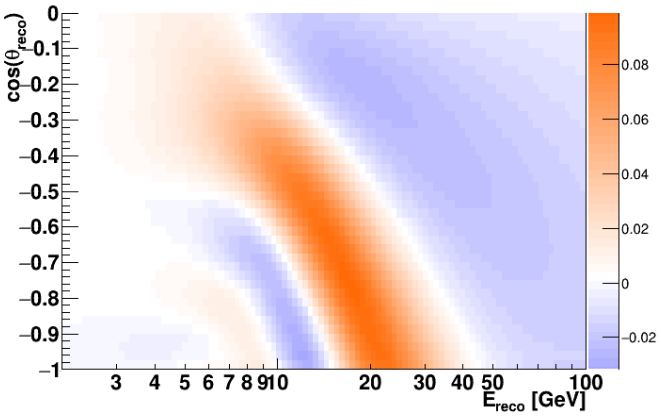

(b) Track-like events

Figure 13: Asymmetries between the atmospheric limit (normal ordering, without energy dependence of γ, see Table 2) and no decoherence on event numbers measured by the detector within three years for the different event topologies. $\cos(\Theta_{reco})$ denotes the reconstructed cosine of the zenith angle, E_{reco} the reconstructed energy of the neutrino.

5.2 Sensitivity to the lowest bounds on decoherence set by MINOS, KamLAND, IceCube and DeepCore

After having understood the path of the neutrino flux information through the detector and its evaluation using asymmetries, in this section we present different asymmetry plots for certain parameters. These parameters were in detail named in section 4.5 and we also gave reasons for using specifically these values.

5.2.1 Energy independent gamma

For an energy independent decoherence parameter and normal ordering the results for solar limit 1 and 2 look similar to the ones we got for the atmospheric limit. The structures look quite similar and also the size of the asymmetries is comparable (for shower-like events up to $\pm 3\,\%$, for track-like events up to $8\,\%$). For inverted ordering the structures and magnitudes mainly remain comparable, only slight deviations can be observed. The detailed asymmetry plots can be found in Figure 14 and Figure 15.

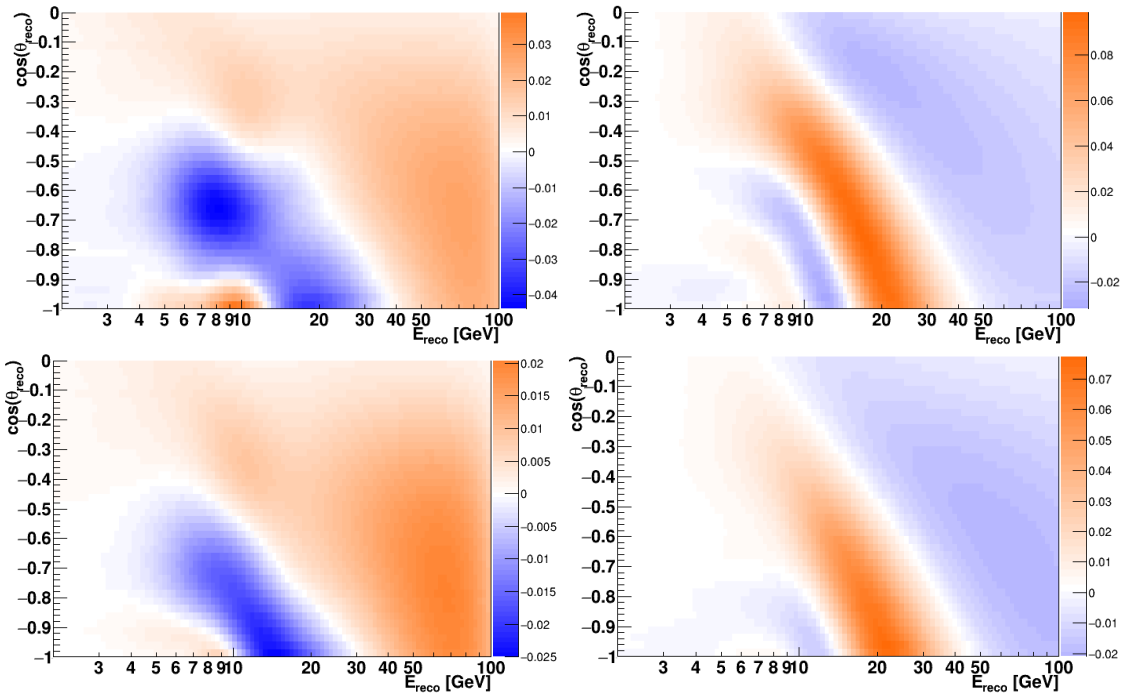

Figure 14: Asymmetry for atmospheric limit and no decoherence using an energy independent γ (see Table 2). Upper row: normal ordering, shower-like events (left) and track-like events (right). Lower row: inverted ordering, shower-like events (left) and track-like events (right).

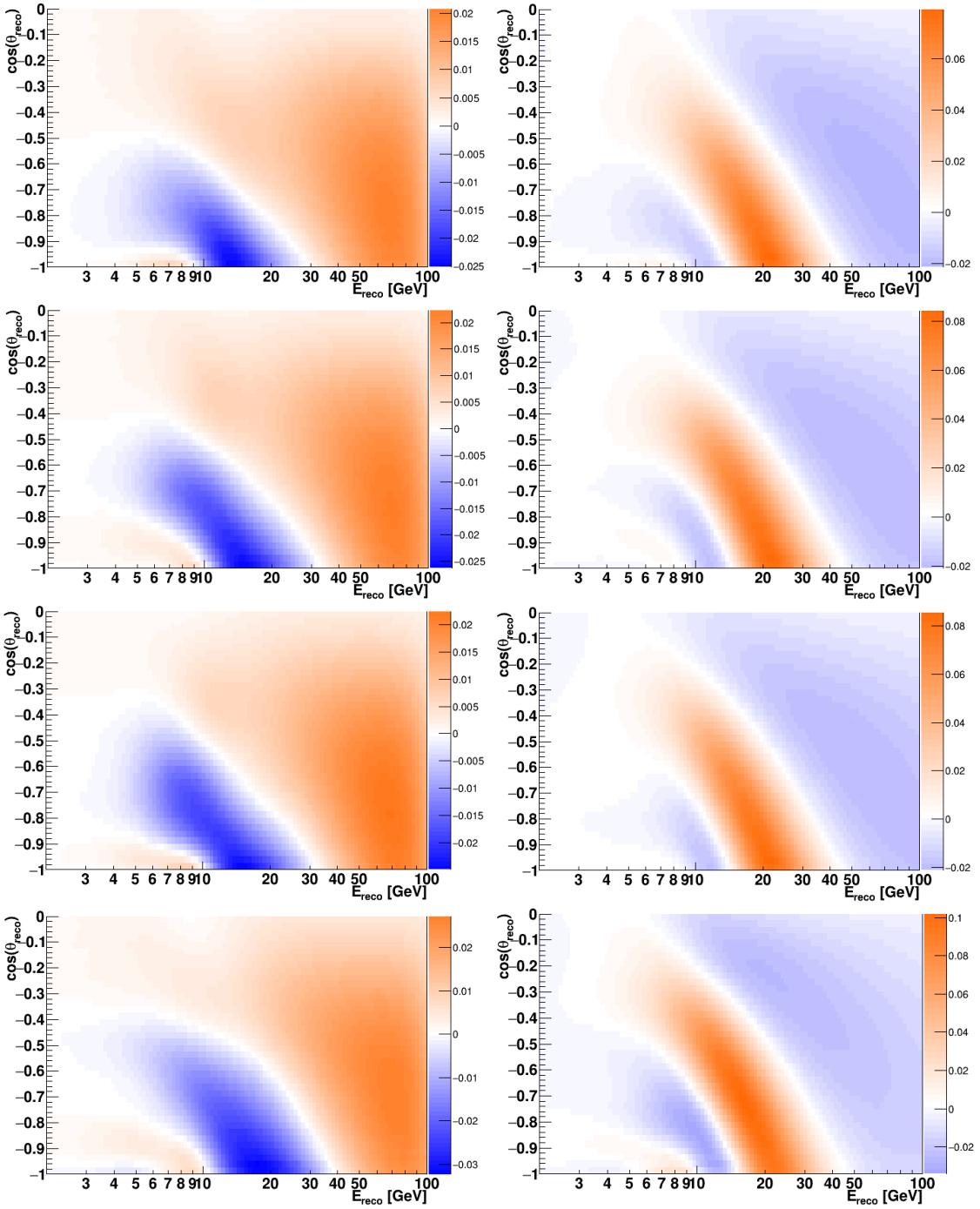

Figure 15: Asymmetry for solar limit 1 / 2 and no decoherence using energy independent γ (see Table 2). Left column: shower-like events for solar limit 1 (normal ordering, inverted ordering) and for solar limit 2 (normal ordering, inverted ordering). Right column: analogously for track-like events.

5.2.2 Power law for dependency of gamma on energy with exponent -1

For γ depending on the energy in a power law with exponent -1, we get a larger spread in the asymmetries. While the atmospheric limit provides us with asymmetries that are larger than 50 % in some cases, the solar limit 2 gives asymmetries of only a few per mille. This is due to the fact that in this limit, the considered decoherence parameter is almost two orders of magnitude smaller than the one for atmospheric and first solar limit (see Table 2). So we give here only the asymmetry plots for the atmospheric limit, as they are the most pronounced ones, see Figure 16. For the others, we reference to the analysis in Section 6.1.

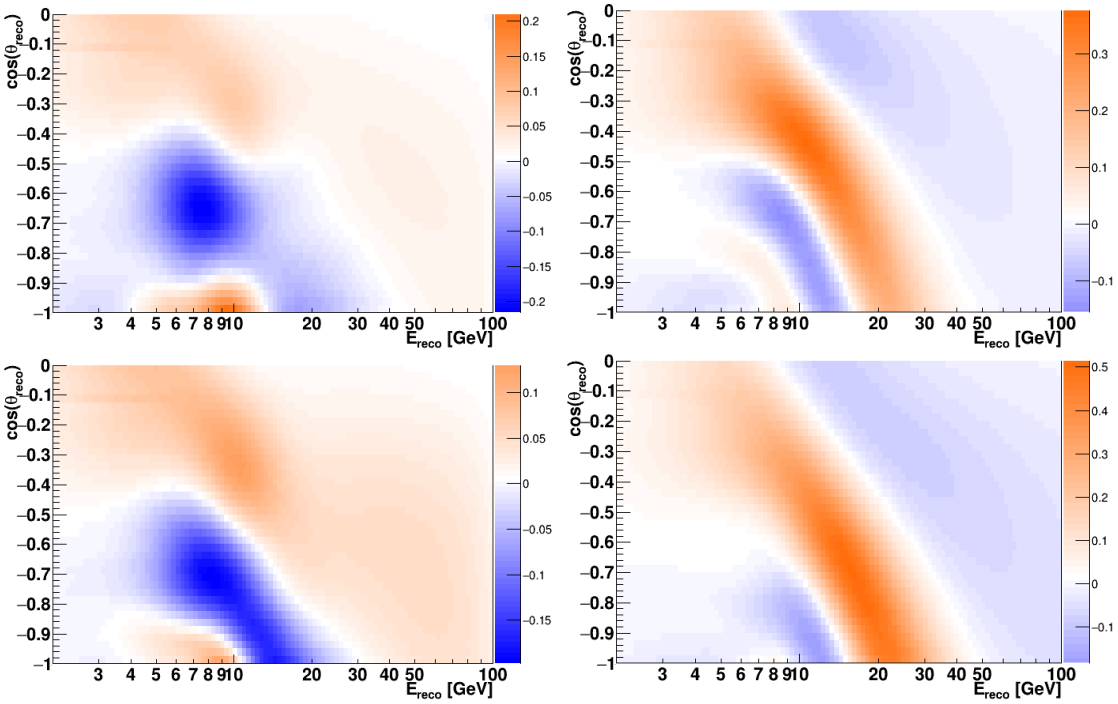

Figure 16: Asymmetry for atmospheric limit and no decoherence using $\gamma \propto E^{-1}$ (see Table 2). Upper row: normal ordering, shower-like events (left) and track-like events (right). Lower row: inverted ordering, shower-like events (left) and track-like events (right).

5.2.3 Power law for dependency of gamma on energy with exponent -2

This case gives the highest asymmetries compared to the other considered parameter sets. The calculated asymmetries are in some parts of the limits more than 80 %. This high sensitivity arises from two main reasons. On the one hand, the given upper boundaries for the decoherence parameter are of the order of 10^{-20} and therefore several orders of magnitude larger than the bounds given for the other exponents of the power law. On the other hand, this is an energy range where ORCA has good sensitivity due to its geometry. As the observed energy range of ORCA centers around 10 GeV, the decoherence effect will be of the order (see for example (36)):

$$\Gamma \cdot L = \gamma \left(\frac{E}{\mathrm{GeV}}\right)^{-2} \cdot L \approx 10^{-22} \cdot 10^{7}\ \mathrm{GeV\ m} \approx 10^{-6}\ \mathrm{eV\ m} \approx 10\ , \tag{41}$$

where we used the propagation length L of the neutrinos instead of the propagation time t in equation (36). As ORCA works with atmospheric neutrinos, this propagation length L is roughly the diameter of the earth. In addition, we used that in natural units $1\ \mathrm{eV} \approx 0.5 \cdot 10^{7}\ \mathrm{m}$. Decoherence enters the oscillations in terms of the additional factor $e^{-\Gamma t} \approx e^{-10}$, which clearly changes the outcome and is well measurable by ORCA. In Figure 17 and Figure 18 the asymmetries for the case of $\gamma \propto E^{-2}$ are plotted.

5.2.4 Power law for dependency of gamma on energy with exponent 1 or 2

Here, the geometry and size of ORCA as well as the upper boundaries given in Table 2, which are very low compared to the other cases, make it impossible to gain new information for these two cases with ORCA. Performing a simple estimate similar to (41) using the highest upper bound for each case (that is 10^{-27} for $\gamma \propto E$ and 10^{-31} for $\gamma \propto E^2$) and 100 GeV as reference energy for ORCA, so the highest observable energy, we get for $\gamma \propto E$

$$\Gamma \cdot L = \gamma \left(\frac{E}{\mathrm{GeV}}\right)^{1} \cdot L \approx 10^{-25} \cdot 10^{7}\ \mathrm{GeV\ m} \approx 10^{-9}\ \mathrm{eV\ m} \approx 10^{-2}\ , \tag{42}$$

and for $\gamma \propto E^2$

$$\Gamma \cdot L = \gamma \left(\frac{E}{\mathrm{GeV}}\right)^{2} \cdot L \approx 10^{-27} \cdot 10^{7}\ \mathrm{GeV\ m} \approx 10^{-11}\ \mathrm{eV\ m} \approx 10^{-4}\ . \tag{43}$$

So, for both cases the decoherence effect is orders of magnitude smaller than for the other cases (see for example (41)). Thus ORCA cannot provide new information if gamma depends on E or E^2. But KM3NeT also provides access to these cases: ARCA, which is sensitive to higher energies than ORCA, may be able to address the energy

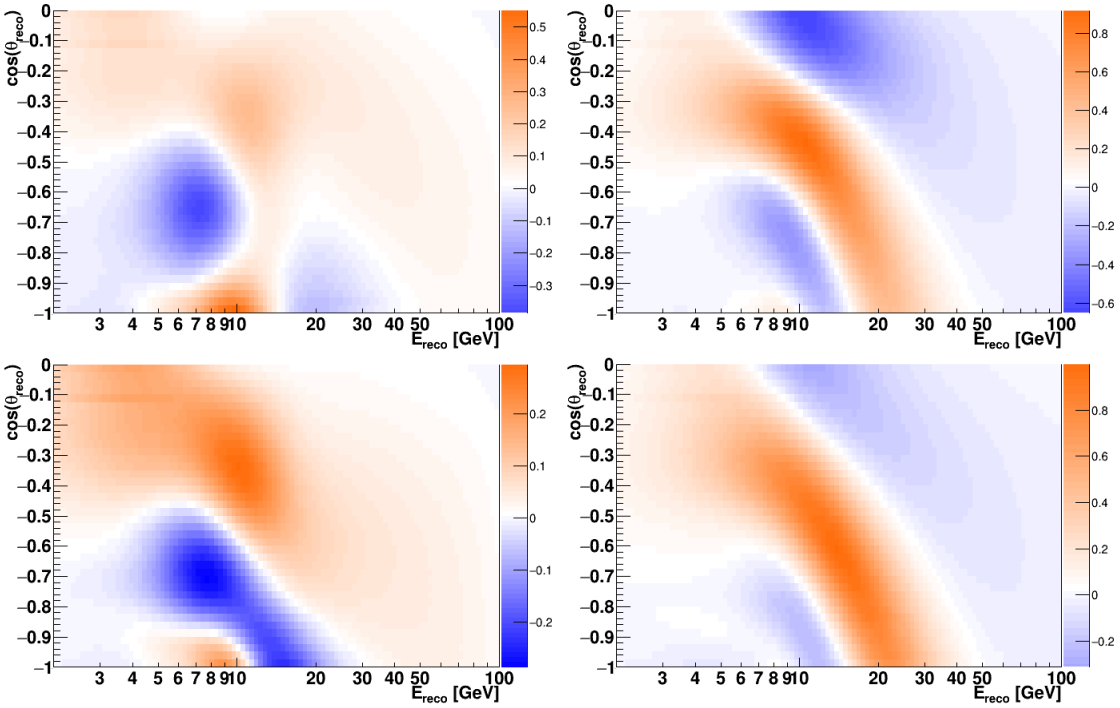

Figure 17: Asymmetry for atmospheric limit and no decoherence using an $\gamma \propto E^{-2}$ (see Table 2). Upper row: normal ordering, shower-like events (left) and track-like events (right). Lower row: inverted ordering, shower-like events (left) and track-like events (right).

regimes needed to work with these two cases and to look for decoherence effects there. In ARCA, L increases from 10^7 m (once through the Earth) up to $10^{20} - 10^{25}$ m, so we would expect a lot of new information on decoherence in this region. Unfortunately, this is compensated by the very low flux (and thus bad statistics) of astrophysical neutrinos that arrive at the detector from such distances (see [35] for more information on quantum decoherence of high-energy neutrinos). However, a sensitivity study for ARCA is outside the scope of this project.

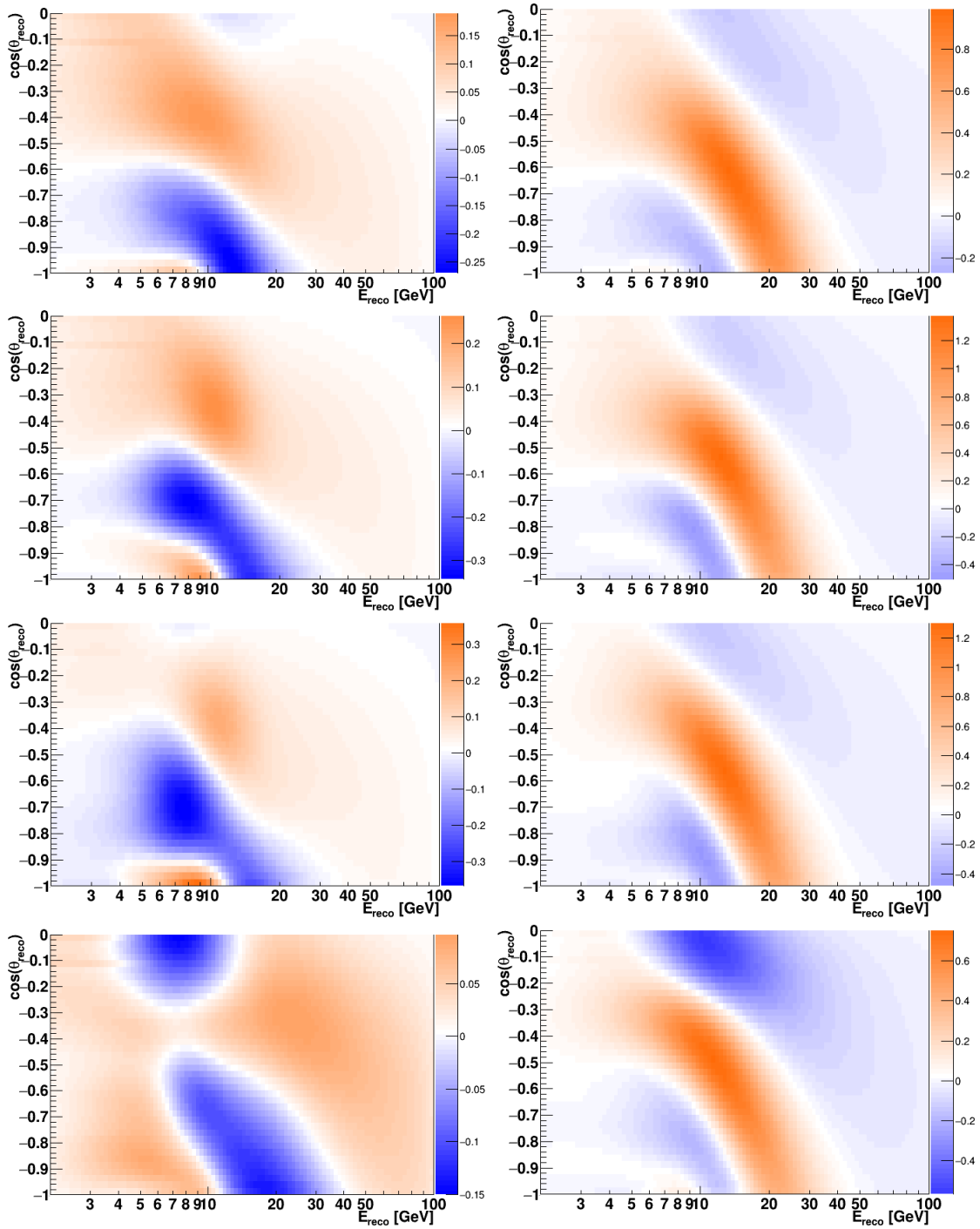

Figure 18: Asymmetry for solar limit 1 / 2 and no decoherence using $\gamma \propto E^{-2}$ (see Table 2). Left column: shower-like events for solar limit 1 (normal ordering, inverted ordering) and for solar limit 2 (normal ordering, inverted ordering). Right column: analogously for track-like events.

6 Sensitivity of ORCA to quantum decoherence

In this section we present and discuss the sensitivity of ORCA to quantum decoherence. We analyse the sensitivity of ORCA on simulated data to see if detailed analyses can provide us with new lower bounds on the decoherence parameters. To achieve this, we first analyse the sensitivity to the decoherence parameter and then test the dependence of the sensitivity on the mixing angle Θ_{23}.

6.1 Sensitivity to the decoherence parameter

In the last step of the project we tested the sensitivity of ORCA to the decoherence parameter γ. We performed the study for normal and inverted ordering and for the five different energy dependencies named above. In the simulation, we worked with data taken during three years and we varied the parameter of γ over several orders of magnitude. For each value we made a fit for each of the three limits, using the same parameters as in the previous section. This generalises the asymmetries obtained in section 5.2. For comparison we also marked the upper bounds from Table 2 with vertical lines. The given values from literature are all on 95 % confidence level (CL), therefore we also used this CL as reference value. The sensitivity analyses were performed using paramNMH. For each ordering, energy dependence of γ and limit, a fit of the oscillogram without decoherence to the one with decoherence was computed. The only fixed constraint was Θ_{13} which is known with good precision. Then the algorithm evaluated the minimum sensitivity by slight variation of the other parameters entering the equations, which are Θ_{23}, δ_{CP}, Δm^2_{32}, the ratios $\frac{\#\bar{\nu}_e}{\#\nu_e}$, $\frac{\#\bar{\nu}_\mu}{\#\nu_\mu}$, $\frac{\#\nu_e}{\#\nu_\mu}$ (where # denotes 'number of'), as well as the ratio between track and shower-like events. The minimisation process is performed by paramNMH using Minuit2 (see [36] for more details).
The minimisation algorithm converged for almost all considered cases. Failures occured at the atmospheric limit with inverted ordering, where the minimisation did not converge for $\gamma \propto E^0$, $\gamma \propto E^1$ and $\gamma \propto E^2$. Nevertheless, the discussions in section 5.2 have shown that these cases are uninteresting for ORCA, as the detector cannot provide new information for them.

Energy independent gamma

For energy independent γ, the analyses resulted in Figure 19. Here, ORCA is not able to improve the limits on the decoherence parameter on a 95 % confidence level. Its sensitivity is comparable to the sensitivity of IceCube for this case.

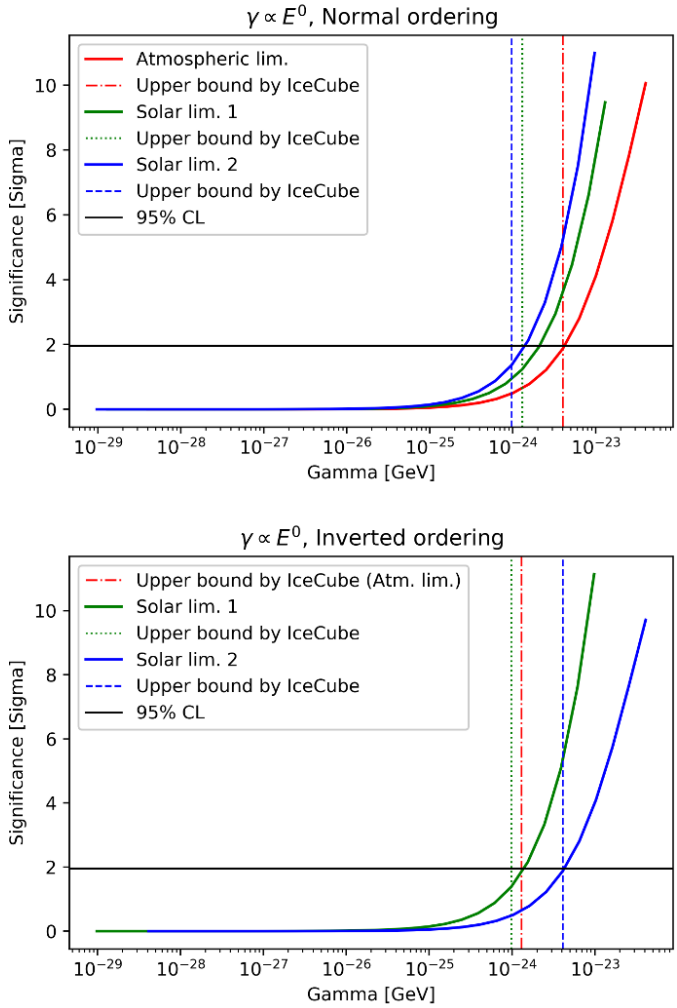

Figure 19: Sensitivity of ORCA to decoherence for energy independent γ. Upper bounds taken from Table 2. Unfortunately, the computation for the atmospheric limit (inverted ordering) did not work correctly, but from section 5.2 follows that there is no new information from ORCA for this limit.

Power law for dependency of gamma on energy with exponent -1

For $\gamma \propto E^{-1}$ ORCA can provide new information for the atmospheric limit and the solar limit 1, which is apparent from Figure 20. This implies that data gathered by ORCA can be analysed in terms of decoherence. If decoherence effects appear, assuming $\gamma \propto E^{-1}$, the parameter must be somewhere within ORCA's sensitivity region below the old upper bound. If no decoherence effects are observed, we are able to lower the upper bound for this case by approximately one order of magnitude. This discussion holds for both normal and inverted ordering, as their behaviour is quite similar for $\gamma \propto E^{-1}$, which is visible in Figure 20. We do not list the exact new values for γ that could be interpolated from the plots, as our analysis was qualitatively, so quantitative values might be misleading.

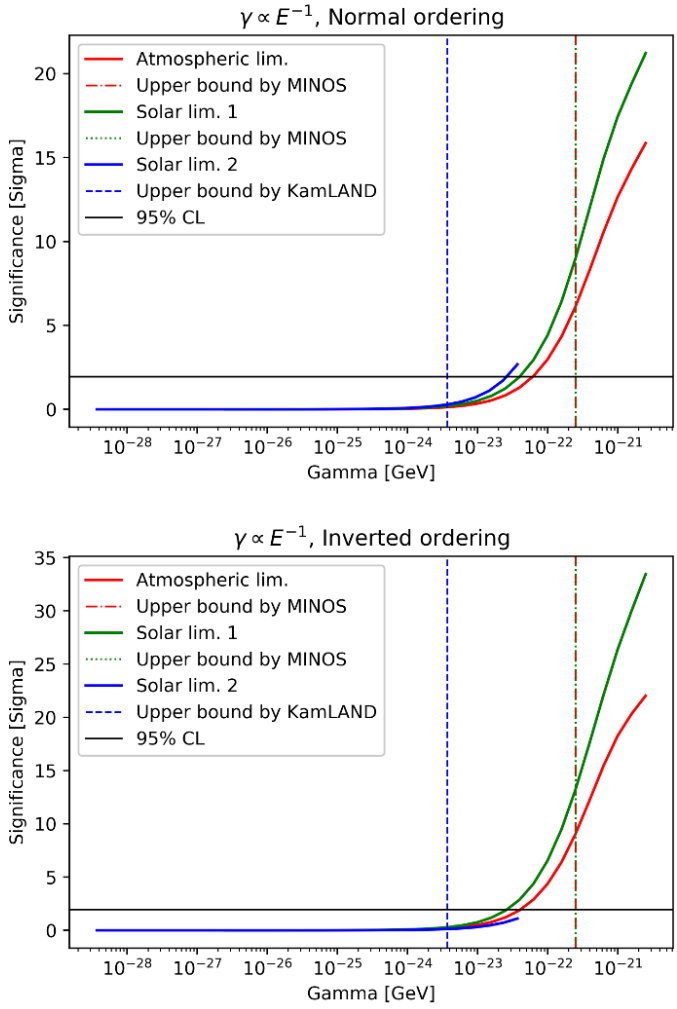

Figure 20: Sensitivity of ORCA to decoherence for $\gamma \propto E^{-1}$. Upper bounds taken from Table 2.

Power law for dependency of gamma on energy with exponent -2

Following from the considerations about the magnitude of decoherence made in section 5.2.3, we expect to get the highest significance for $\gamma \propto E^{-2}$ compared to the other cases. And indeed, as is recognizable in Figure 21, in this case ORCA has a sensitivity of $15\,\sigma$ to $20\,\sigma$ for decoherence at the starting values in Table 2. This implies that we can deliver new input in this case: Either decoherence is measured, or we can set new upper boundaries that are approximately two orders of magnitude smaller than the old ones.

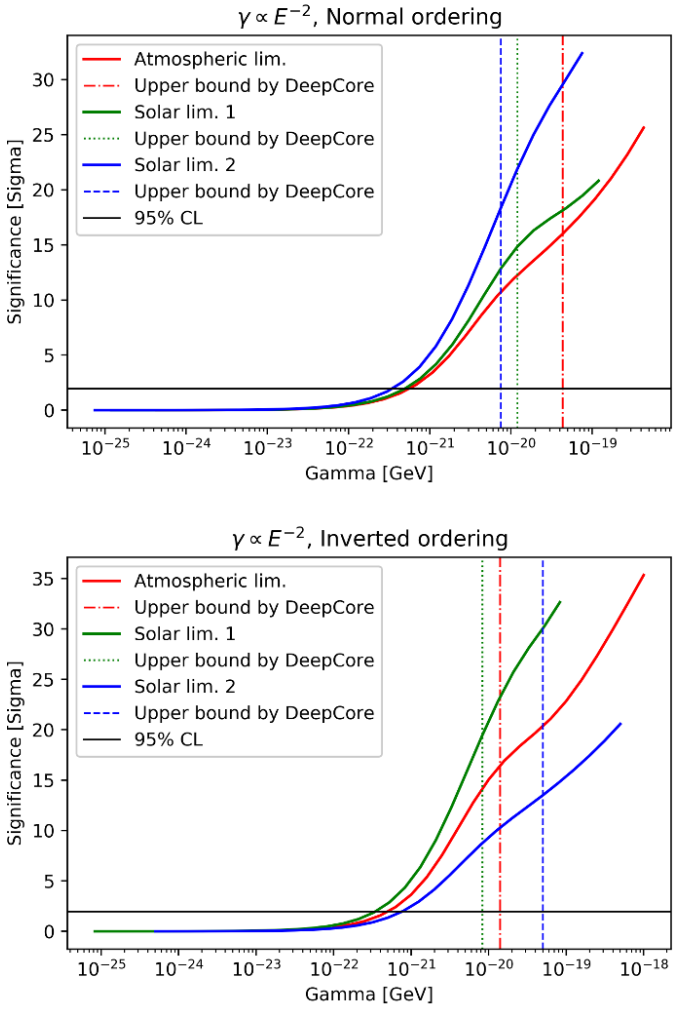

Figure 21: Sensitivity of ORCA to decoherence for $\gamma \propto E^{-2}$. Upper bounds taken from Table 2.

Power law for dependency of gamma on energy with exponent 1 or 2

For $\gamma \propto E$ or $\gamma \propto E^2$ the existing upper bounds for the decoherence parameters are several orders of magnitude below the sensitivity of ORCA, see Figure 22. The reasons for this lie in the geometry of the detector, which has been explained and estimated in section 5.2.4. Therefore no new information can be expected for this parameter set from ORCA.

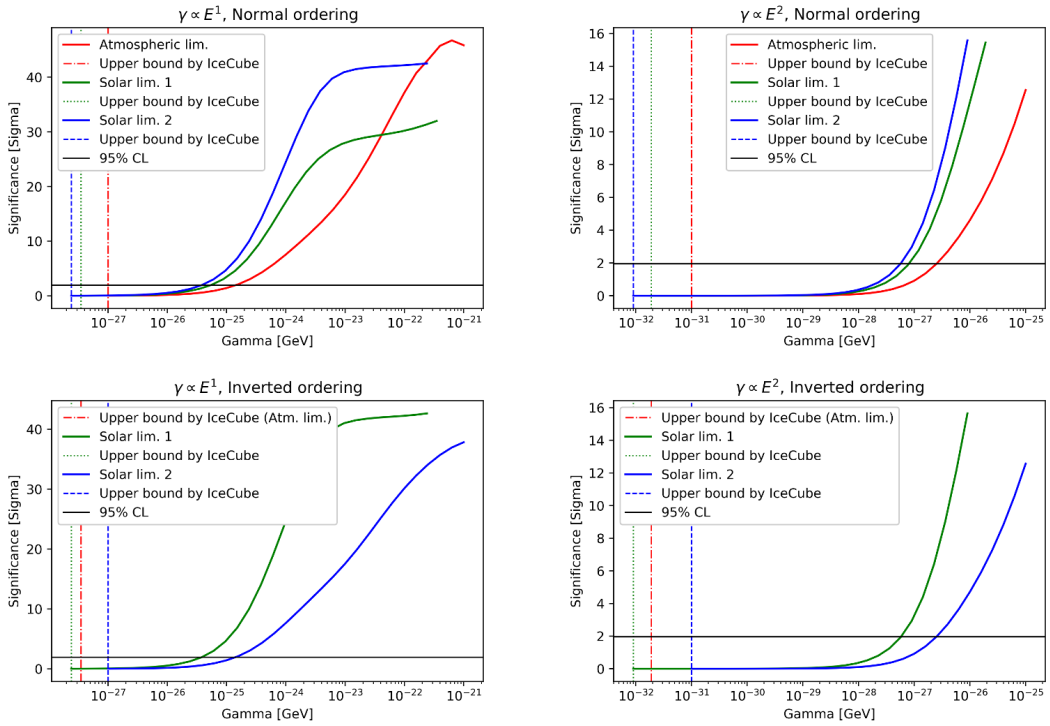

Figure 22: Sensitivity of ORCA to decoherence for $\gamma \propto E^1$ (left column) and $\gamma \propto E^2$ (right column). Upper bounds taken from Table 2. Unfortunately, the computations for the atmospheric limit (inverted ordering) did not work correctly, but from section 5.2 follows that there is no new information from ORCA for these limits.

6.2 Dependence of the sensitivity on the mixing angle Θ_{23}

As a next step we analysed how the sensitivity of ORCA to decoherence depends on the value of Θ_{23}. For previous simulations we assumed $\Theta_{23} = 45°$. We chose this value as the 3σ-range is approximately between 40° and 50° and the best fit value is also fluctuating between these two edges. As Θ_{23} is a crucial parameter for determining the neutrino mass ordering and its value is not known very well, we wanted to test how sensitivity analyses for decoherence may change if a new value for Θ_{23} is fixed. We performed sensitivity analyses for both normal and inverted ordering using the five different cases named above for the energy dependence of γ. The values of γ were assigned according to Table 2. As ORCA is not sensitive to the cases $\gamma \propto E$ and $\gamma \propto E^2$, we are only going to present the results for the other three cases. These results can be seen in Figure 23 for normal ordering and in Figure 24 for inverted ordering.
The sensitivity analyses were performed using paramNMH. For each ordering, energy dependence of γ and limit, a fit of the oscillogram without decoherence to the one with decoherence was computed using each integer value of Θ_{23} between 40° and 50° (boundaries included) as starting point. The only fixed constraint was Θ_{13} which is known with good precision. Then the algorithm evaluated the minimum sensitivity by slight variation of the other parameters entering the equations, which were named in the previous section.
In summary, the highest minima for the sensitivity lie close to 45° for almost all considered cases. So in order to generalise the asymmetries we got and also the sensitivity analyses on γ (which were presented in the previous section), we have to lower the sensitivity of our results slightly, depending on the most recent best fit value of Θ_{23}. Nevertheless, the decrease of sensitivity is for most cases lower than $1\,\sigma$ and in general lower than $2\,\sigma$. Details can be taken from Figure 23 and Figure 24.

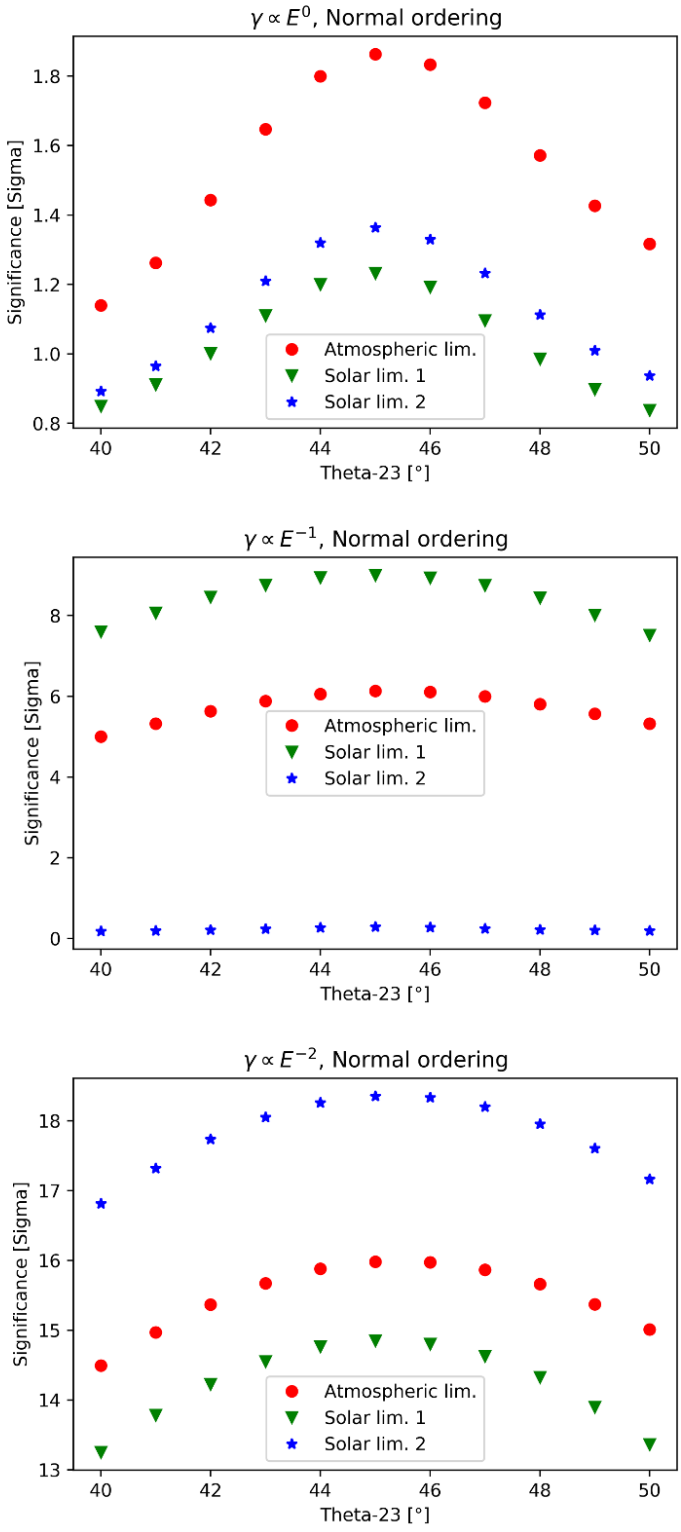

Figure 23: Sensitivity of decoherence to Θ_{23} for normal ordering. The values of γ were taken from Table 2.

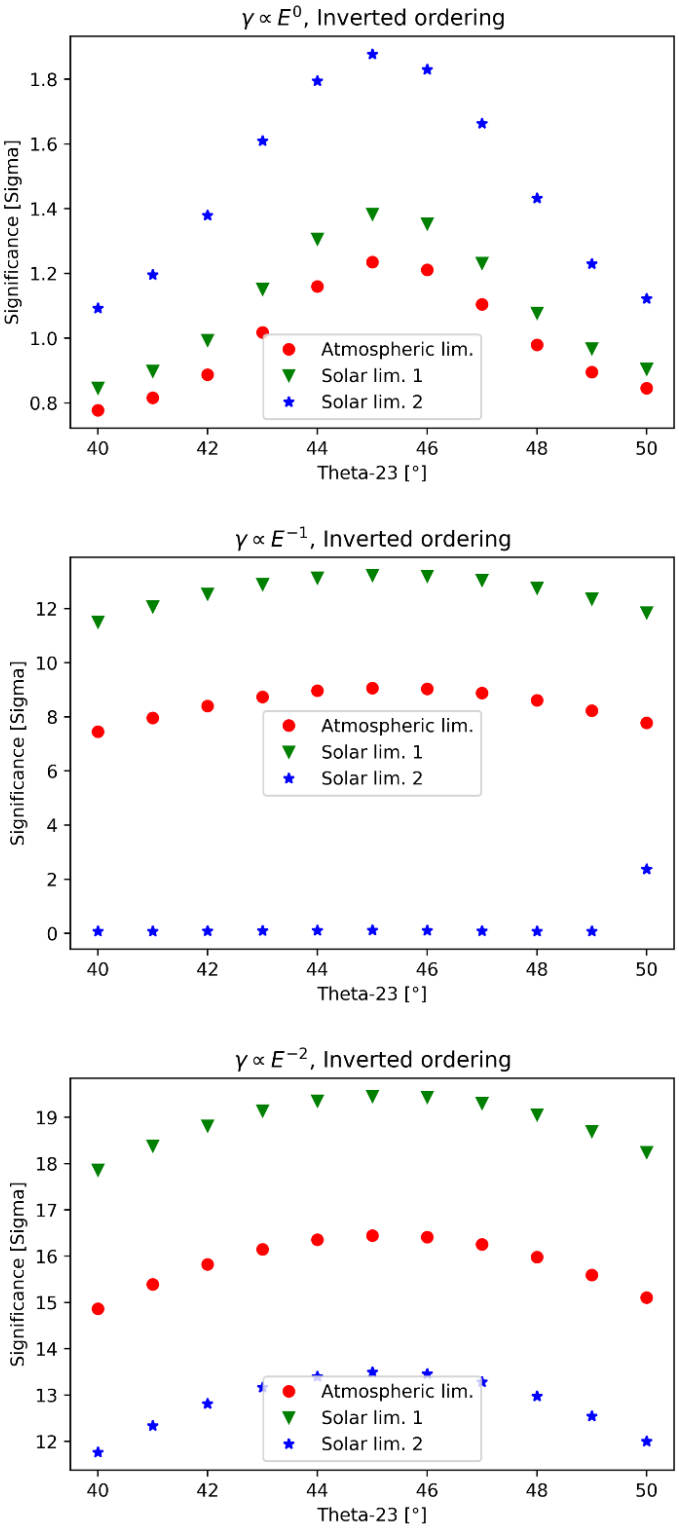

Figure 24: Sensitivity of decoherence to Θ_{23} for inverted ordering. The values of γ were taken from Table 2.

7 Conclusion and Outlook

Within the research project we performed a first analysis whether ORCA can give new insights into non-classical decoherence effects of neutrinos. Using a simple model, we modified existing analysis tools and made a systematic study for a small specific parameter room. This particular choice of parameters was motivated and we were able to deduce predictions for a fairly high volume of the parameter space from it. Our computations showed that ORCA gives new information on quantum decoherence of neutrino systems and that therefore more detailed analyses promise to be fruitful. To conclude, in this project we found out that ORCA is an influential player in the detection of decoherence and we get new knowledge on decoherence with data gathered by ORCA.
Due to its geometry, we found that ARCA might be a complementary supplement. Thus KM3NeT should be able to deliver new values for almost the entire parameter space of the decoherence parameters.

Possible extensions of the project include a more complex model for decoherence than the one we applied, for example one could try to drop the condition of energy conservation. This gives rise to many new, unknown decoherence parameters. But detailed investigations of the new parameter space may give certain limits where only few independent parameters remain, as it was the case for our analysis. Also a systematic analysis of the parameter space we used is productive. When performing the fits to determine the sensitivity of ORCA to quantum decoherence effects, we assumed that the dependency has similar behaviour like the sensitivity to the neutrino mass ordering on Θ_{23}. This is a priori not justified, but detailed analyses of the parameter space and its behaviour when investigating decoherence require significantly more time.

As decoherence might have an essential influence on the neutrino oscillation parameters we measure and also might give access to quantum gravity theories, it is of high importance to continue research on this topic.

8 Appendix

Values for the 44 layer PREM

Radius (km)	Density ($10^3 kg/m^3$)	Z/A	Layer
200.0	13.088	0.4691	Inner Core
400.0	13.080	0.4691	
600.0	13.054	0.4691	
800.0	13.010	0.4691	
1000.0	12.949	0.4691	
1200.0	12.871	0.4691	
1221.5	12.775	0.4691	
1400.0	12.166	0.4691	Outer Core
1600.0	12.069	0.4691	
1800.0	11.947	0.4691	
2000.0	11.809	0.4691	
2200.0	11.655	0.4691	
2400.0	11.483	0.4691	
2600.0	11.293	0.4691	
2800.0	11.083	0.4691	
3000.0	10.853	0.4691	
3200.0	10.602	0.4691	
3400.0	10.327	0.4691	
3480.0	10.029	0.4691	
3600.0	5.566	0.4954	Mantle
3630.0	5.506	0.4954	
3800.0	5.491	0.4954	
4000.0	5.407	0.4954	
4200.0	5.307	0.4954	
4400.0	5.207	0.4954	
4600.0	5.106	0.4954	
4800.0	5.003	0.4954	
5000.0	4.898	0.4954	
5200.0	4.790	0.4954	
5400.0	4.678	0.4954	
5600.0	4.563	0.4954	
5701.0	4.443	0.4954	
5771.0	3.992	0.4954	Crust, Sea,
5871.0	3.976	0.4954	and Atmosphere
5971.0	3.850	0.4954	
6061.0	3.543	0.4954	
6151.0	3.490	0.4954	
6221.0	3.360	0.4954	
6291.0	3.367	0.4954	
6346.6	3.375	0.4954	
6356.0	2.900	0.4956	
6368.0	2.600	0.4956	
6371.0	1.027	0.5525	
6386.0	0.001	0.4991	

References

[1] C. L. Cowan, F. Reines, F. B. Harrison, H. W. Kruse, and A. D. McGuire. Detection of the free neutrino: a confirmation. *Science*, 124(3212):103–104, 1956. URL http://science.sciencemag.org/content/124/3212/103.

[2] http://www.neutrino.uni-hamburg.de/sites/site_neutrino/content/e45939/e48540/e48541/e48544/infoboxContent48545/material-vorlesung1-moessbauer-pauli.pdf. Accessed: 2018-10-29.

[3] E. Fermi. Versuch einer Theorie der β-Strahlen. I. *Zeitschrift für Physik*, 88(3): 161–177, 1934. URL https://doi.org/10.1007/BF01351864.

[4] Fred L. Wilson. Fermi's theory of beta decay. *American Journal of Physics*, 36(12): 1150–1160, 1968. URL https://doi.org/10.1119/1.1974382.

[5] Raymond Davis, Don S. Harmer, and Kenneth C. Hoffman. Search for neutrinos from the sun. *Phys. Rev. Lett.*, 20:1205–1209, 1968. URL https://link.aps.org/doi/10.1103/PhysRevLett.20.1205.

[6] Bruce T. Cleveland, Timothy Daily, Jr. Raymond Davis, James R. Distel, Kenneth Lande, C. K. Lee, Paul S. Wildenhain, and Jack Ullman. Measurement of the solar electron neutrino flux with the homestake chlorine detector. *The Astrophysical Journal*, 496(1):505, 1998. URL http://stacks.iop.org/0004-637X/496/i=1/a=505.

[7] Raymond Davis. A review of the homestake solar neutrino experiment. *Progress in Particle and Nuclear Physics*, 32:13 – 32, 1994. URL http://www.sciencedirect.com/science/article/pii/0146641094900043.

[8] V. Gribov and B. Pontecorvo. Neutrino astronomy and lepton charge. *Physics Letters B*, 28(7):493 – 496, 1969. URL http://www.sciencedirect.com/science/article/pii/0370269369905255.

[9] L. Wolfenstein. Neutrino oscillations in matter. *Phys. Rev. D*, 17:2369–2374, 1978. URL https://link.aps.org/doi/10.1103/PhysRevD.17.2369.

[10] Y. et al. Fukuda. Evidence for oscillation of atmospheric neutrinos. *Phys. Rev. Lett.*, 81:1562–1567, 1998. URL https://link.aps.org/doi/10.1103/PhysRevLett.81.1562.

[11] John N. Bahcall, M. Concepcion Gonzalez-Garcia, and Carlos Peña-Garay. Solar neutrinos before and after kamland. *Journal of High Energy Physics*, 2003(02):009, 2003. URL http://stacks.iop.org/1126-6708/2003/i=02/a=009.

[12] http://www.nu-fit.org/. Accessed: 2018-10-29.

[13] T. Eberl et al. Letter of intent for KM3NeT 2.0. *J. Phys.*, G43(8):084001, 2016. URL https://arxiv.org/abs/1601.07459.

[14] http://www.km3net.org/. Accessed: 2018-11-10.

[15] João A. B. Coelho and W. Anthony Mann. Decoherence, matter effect, and neutrino hierarchy signature in long baseline experiments. *Phys. Rev. D*, 96:093009, 2017. URL https://link.aps.org/doi/10.1103/PhysRevD.96.093009.

[16] Dean Morgan, Elizabeth Winstanley, Jurgen Brunner, and Lee F. Thompson. Probing quantum decoherence in atmospheric neutrino oscillations with a neutrino telescope. *Astroparticle Physics*, 25(5):311 – 327, 2006. URL http://www.sciencedirect.com/science/article/pii/S0927650506000338.

[17] E. Lisi, A. Marrone, and D. Montanino. Probing possible decoherence effects in atmospheric neutrino oscillations. *Phys. Rev. Lett.*, 85:1166–1169, 2000. URL https://link.aps.org/doi/10.1103/PhysRevLett.85.1166.

[18] Fabio Benatti and Roberto Floreanini. Open system approach to neutrino oscillations. *Journal of High Energy Physics*, 2000(02):032, 2000. URL http://stacks.iop.org/1126-6708/2000/i=02/a=032.

[19] Marcelo M. Guzzo, Pedro C. de Holanda, and Roberto L.N. Oliveira. Quantum dissipation in a neutrino system propagating in vacuum and in matter. *Nuclear Physics B*, 908:408 – 422, 2016. URL http://www.sciencedirect.com/science/article/pii/S0550321316300682.

[20] G. Balieiro Gomes, D. V. Forero, M. M. Guzzo, P. C. De Holanda, and R. L. N. Oliveira. Quantum Decoherence Effects in Neutrino Oscillations at DUNE. 2018. URL https://arxiv.org/abs/1805.09818.

[21] Pilar Coloma, Jacobo Lopez-Pavon, Ivan Martinez-Soler, and Hiroshi Nunokawa. Decoherence in neutrino propagation through matter, and bounds from icecube/deepcore. *arXiv preprint arXiv:1803.04438*, 2018. URL https://arxiv.org/abs/1803.04438.

[22] Joao de Abreu Barbosa Coelho. *Investigacao de Mecanismos Alternativos a Oscilacao de Neutrinos no Experimentos MINOS*. PhD thesis, Campinas State U., 2012. URL http://lss.fnal.gov/archive/thesis/2000/fermilab-thesis-2012-23.pdf.

[23] Christopher Stover. "Gell-Mann Matrix." From MathWorld–A Wolfram Web Resource, created by Eric W. Weisstein. http://mathworld.wolfram.com/Gell-MannMatrix.html. Accessed: 2018-11-01.

[24] G. Lindblad. On the generators of quantum dynamical semigroups. *Comm. Math. Phys.*, 48(2):119–130, 1976. URL https://projecteuclid.org:443/euclid.cmp/1103899849.

[25] F. Benatti and R. Floreanini. Completely positive dynamical maps and the neutral kaon system. *Nuclear Physics B*, 488(1):335 – 363, 1997. URL http://www.sciencedirect.com/science/article/pii/S0550321396007122.

[26] G. Lindblad. On the generators of quantum dynamical semigroups. *Communications in Mathematical Physics*, 48(2):119–130, 1976. URL https://doi.org/10.1007/BF01608499.

[27] F. Benatti and H. Narnhofer. Entropy behaviour under completely positive maps. *Letters in Mathematical Physics*, 15(4):325–334, 1988. URL https://doi.org/10.1007/BF00419590.

[28] J. Hofestädt, C. W. James, and et al. Intrinsic limits on resolutions in muon- and electron-neutrino charged-current events in the km3net/orca detector. *Journal of High Energy Physics*, 2017(5), 2017. URL https://doi.org/10.1007/JHEP05(2017)008.

[29] Adam M. Dziewonski and Don L. Anderson. Preliminary reference earth model. *Physics of the Earth and Planetary Interiors*, 25(4):297 – 356, 1981. URL http://www.sciencedirect.com/science/article/pii/0031920181900467.

[30] https://github.com/joaoabcoelho/OscProb. Accessed: 2018-11-12.

[31] https://root.cern.ch/. Accessed: 2018-11-12.

[32] http://www.icrr.u-tokyo.ac.jp/~mhonda/nflx2014/index.html. Accessed: 2019-01-12.

[33] R. L. N. Oliveira, M. M. Guzzo, and P. C. de Holanda. Quantum dissipation and *cp* violation in minos. *Phys. Rev. D*, 89:053002, 2014. URL https://link.aps.org/doi/10.1103/PhysRevD.89.053002.

[34] G. Balieiro Gomes, M. M. Guzzo, P. C. de Holanda, and R. L. N. Oliveira. Parameter limits for neutrino oscillation with decoherence in kamland. *Phys. Rev. D*, 95:113005, 2017. URL https://link.aps.org/doi/10.1103/PhysRevD.95.113005.

[35] Dan Hooper, Dean Morgan, and Elizabeth Winstanley. Probing quantum decoherence with high-energy neutrinos. *Physics Letters B*, 609(3):206 – 211, 2005. URL http://www.sciencedirect.com/science/article/pii/S0370269305000833.

[36] https://root.cern.ch/root/htmldoc/guides/minuit2/Minuit2.html. Accessed: 2019-02-01.